sustainability

MDPI

Article

Sustainability Evaluation of the Al-Qasab Playa by Integrating Hydrogeochemical and Graphical, ArcGIS Watershed, and Thermodynamic Geochemical Modeling Approaches

Hassan E. Gomaa [1,2,3,*], Fatma A. Gomaa [1,4], Sami M. Abdel Azeem [3,5,6] and Abdullah A. Alotaibi [1,3,*]

1 Department of Chemistry, College of Science and Humanities, Shaqra University, Ad-Dawadmi 11911, Saudi Arabia; fjomaah@su.edu.sa
2 Department of Nuclear Safety Engineering, Nuclear Installations Safety Division, Atomic Energy Authority, Cairo 11765, Egypt
3 Water Research Group, College of Science and Humanities at Ad-Dawadmi, Shaqra University, Ad-Dawadmi 11911, Saudi Arabia; sma13@fayoum.edu.eg or sami_a@su.edu.sa
4 Department of Chemistry, College of Women for Science, Arts, and Education, Ain Shams University, Cairo 11757, Egypt
5 Chemistry Department, College of Science and Humanities, Shaqra University, Al-Quwayiyah 11971, Saudi Arabia
6 Chemistry Department, Faculty of Science, Fayoum University, Fayoum 63514, Egypt
* Correspondence: hjomaah@su.edu.sa or hassan_emgh@yahoo.com (H.E.G.); aaalotaibi@su.edu.sa (A.A.A.)

Abstract: Drawing development plans requires evaluating the available resources and assessing their sustainable and subsequent utilization-driven environmental impacts. The current work is concerned with evaluating the sustainability of the halite harvesting process from Al-Qasab Playa, Shaqra, Central Saudi Arabia. The authors integrated, conceptually and quantitatively, ArcGIS-processed SRTM-DEM (Shuttle Radar Topography Mission-Digital Elevation Model) data, hydrogeochemical and thermodynamic-based geochemical modelling, and graphical approaches to achieve the ultimate aims of the study. The watershed is identified as a nonmarine closed basin with a drainage area of 1290 km^2, with the slope controlling recharge to the Playa. The Chadha plot including the rainwater exhibits linear regression, with an R^2 value of 0.9947, confirming the rainwater origin of the Playa water. The hardness-forming ions are primarily removed in pond 3, eliminating the need for costly and power-consuming steps of softening with ion exchange resins or nanofiltration as it can be used directly as a readily available feed for the chlor-alkali process for producing NaOH, Cl_2, and H_2 gases through electrolysis. XRD (X-ray diffraction) analysis and the SEM-EDS (Scanning electron microscopy-energy dispersive X-ray spectroscopy) of the harvested halite confirmed its purity. An improved design of the current folkloric harvesting process has been proposed based on the saturation indices calculated thermodynamically to provide a readily available feed intake for the electrolysis chlor-alkali process with or without minimal pretreatment to produce higher value chemicals. The methodological aspects presented here are deemed robust and valid for applications in other study areas, including the assessment of the exploitation of the rejected brine from the desalination plants to achieve the zero liquid discharge approach, as well as other types of sabkhas, regardless of their geographical location.

Keywords: Inland Playa; salt marches; evaporation; Saudi Arabia; halite harvesting; PhreeqC; brines; watershed

Citation: Gomaa, H.E.; Gomaa, F.A.; Abdel Azeem, S.M.; Alotaibi, A.A. Sustainability Evaluation of the Al-Qasab Playa by Integrating Hydrogeochemical and Graphical, ArcGIS Watershed, and Thermodynamic Geochemical Modeling Approaches. *Sustainability* **2024**, *16*, 2118. https://doi.org/10.3390/su16052118

Academic Editor: Alan Randall

Received: 8 February 2024
Revised: 26 February 2024
Accepted: 28 February 2024
Published: 4 March 2024

1. Introduction

1.1. Playas in Saudi Arabia

The preservation of water resource quality and the development of sustainable development plans, especially those concerning exploring and exploiting the available natural resources, are of the highest priorities of the Kingdom of Saudi Arabia (KSA) to realize the

2030 Vision. Saudi Arabia Vision 2030 is a government program launched (first announced on 25 April 2016) by the Kingdom of Saudi Arabia to increase economic, social, and cultural diversification. It has developed a vision based on three pillars, including a vital society, a thriving economy, and an ambitious nation, through which the Kingdom will use its investment power to create a more diverse and sustainable economy. Resource exploration and sustainable utilization, to which the current work is aligned, are one of the primary strategic objectives of the 2030 Vision. Identifying the potential investment opportunities and assessing their subsequent utilization-driven environmental impacts are equally important. Some of the wadis and low depressions in central Saudi Arabia are covered with salt flats known as inland sabkhas or salt marshes. The aquifers below such sabkhas are prone to receiving substantial recharge from the upper-lying salt flats. So, it is essential to understand these flats' hydrogeochemical processes and geochemistry to explore the impacts on the chemistry beneath the groundwater [1]. In central KSA, numerous closed depressions exist where highly mineralized lakes are formed, locally called "sabkha". These depressions form inland drainage basins for the area around them as water flows from higher to lower altitudes, mainly lying in the central parts of the basin. The drainage water is usually laden with salts as it dissolves more and more salts from the contact with rocks and soil through its trip. The solvation process is exacerbated as the local climate gets hot. When it dries up, damp and salt-encrusted sediments are formed, giving rise to what is known as an inland sabkha [2].

Sabkhas are hypersaline ecosystems with unique characteristics as they have special geological settings, including sedimentology and geochemistry, and extraordinary life conditions (sabkhas are unique ecosystems that are highly saline; hence, specially adapted plants and microbial communities can grow), attracting researchers' interest in understanding their functions [3]. These sabkhas are widespread throughout the Kingdom of Saudi Arabia in eastern, western, and even central regions. From an engineering point of view, in their natural state, sabkha soils are of low density and strength, giving rise to many geotechnical problems due to the susceptibility to strength loss, collapse upon wetting, and high salt content [4]. Thus, in Saudi Arabia, sabkhas are being studied for different purposes; for example, geochemical considerations and the influence of ground and groundwater geochemistry are studied for construction purposes [5,6]. The geochemical and geotechnical characteristics of Abhor subsoil have been studied [7], while Sabtan and Shehata, 2003 studied the Al-Lith coastal sabkha's hydrology [8].

Al-Harbi et al., 2006 stated that some of the low depressions and wadis in central Saudi Arabia are enriched with salts, forming inland sabkhas. The above-ground salt flats may substantially recharge the aquifers below, pointing to the importance of investigating the impacts of the geochemistry and mineralogy of top-laid salt flats on the potentially affected groundwater chemistry [1]. One of the potential impacts is the salinization of the underlying aquifer with the readily soluble minerals that are possibly present in the top-laid salt flats. Ye et al., 2018 studied the salt assemblages precipitated during the evaporation of concentrated brine collected from the Gasikule Salt Lake (GSL) to understand the formation of potassium deposits in the Qaidam Basin [9]. The GSL is one of the saline lakes in the Qaidam basin (covering approximately 120,000 km^2), a hyperarid basin occupying a large part of Haixi Prefecture in Qinghai Province, China. Taj and Aref 2015 studied two saline (halite and gypsum) pans recently developed overlying lagoonal and sabkha sediments in the Sarum area, south Jeddah, Saudi Arabia, as a result of the construction of an asphalt road 30 years ago. The structural and textural characteristics of the halite layers reflect their formation during flooding, evaporative concentration, and desiccation stages of the ephemeral halite pan. Taj and Aref 2015 reported that the flooding stage textures record partial dissolution of the halite crusts, forming truncation surfaces, microkarst pits, pipes, and vugs [10]. Attia 2013 studied the sedimentological characteristics and geochemical evolution of the Nabq Sabkha, Gulf of Aqaba, Sinai, Egypt. He concluded that the high salinity values are due to the area's aridity, favoring halite precipitation. He used comparative sedimentological, chemical,

and mineralogical methods to help interpret paleo-depositional environments of ancient evaporite sequences, which are still debated [11]. Manning and Aranovich 2014 reviewed the brines' thermodynamic, petrologic, and geochemical effects at high pressure and temperature [12]. They concluded several observations of brine participation in high-grade metamorphic processes, including findings of alkali and alkaline-earth halides as daughter crystals in fluid inclusions; appreciable concentrations of Cl^- measured in amphiboles, biotite, scapolite, and apatite; and direct observations of high-temperature halides present in the intergranular space in high-grade rocks [12].

Sabtan and Shehata 2002 mentioned the problems that may be associated with sabkhas, such as strength reduction and soil subsidence during the dissolution of salts, corrosive action caused by the high salinity of the soil and groundwater, and heave during salt recrystallisation [6,13]; flooding because of the low infiltration rate of sabkha soil; and groundwater rise in already urbanized areas [6,8]. The magnitude of such hazards in the sabkhas depends upon various geomorphic, geologic, and hydrogeologic settings. Therefore, any sabkha's geomorphology, geology, and hydrogeology must be investigated before any development effort occurs [8]. Hussain et al., 2020 conducted an interesting study on the geochemistry and isotopic analysis of brines in the coastal sabkhas in the eastern region of the Kingdom of Saudi Arabia. They proposed several solute-source models to elucidate the origin of the solutes in the Gulf coastal Sabkhas. The Cl^- and Br^- relationship was used to assess the source of solutes in combination with the activities of ^{226}Ra and the bromine isotope $\delta^{11}Br$. The possible origin of water in the system was identified using the isotopes of $\delta^{18}O$ and $\delta^{2}H$ and the activity of ^{3}H [14]. Recently, Saeed et al., 2021 researched the chemical evolution of an inland sabkha, Sabkha Matti (SM). Sabkha Matti in Saudi Arabia is a potential discharge point for regional groundwater systems in the Rub' al Khali topographic basin of Saudi Arabia. He studied the hydrogeochemical evolution of this sabkha (salt flat) and the underlying aquifers using a combination of geological, hydraulic, hydrochemical, and isotopic approaches to assess the hydrogeochemical evolution of SM to evaluate its impact on the regional aquifer systems [15].

There are many such sabkhas in central Saudi Arabia, such as Al-Awshaziyah Sabkha, which lies between 26°15′00″ N and 44°15′00″ E on the Riyadh-Al-Madinah Al-Munawarrah main road, about 25 km from Unayzah city in the Al-Qassem region. The second major one is the Al-Qasab Sabkha, an inland salt marsh in the village of Al-Qasab, which administratively belongs to Shaqra Governorate, about 150 km northwest of Riyadh's capital between E 45°29′0″ and 45°35′0″ and N 25°13′0″ and 25°20′0″ in the northern hemisphere WGS84/UTM zone 37N. It is famous for producing over one-third of the Kingdom's need for coarse salt extracted from the ground. Al-Qasab is walled with a mud barrier measuring four meters or more and a width of about two meters. Al-Qasab's climate is hot, with temperatures varying between 40 and 50 °C during summer, giving rise to maximum evaporation. It is arid, with less than 10 mm of average annual rainfall. It is generally plain, with an average altitude of 640 m above sea level. Recently, digital elevation model (DEM) data representing the elevation or topography of the earth's surface have been widely utilized for environmental studies, including catchment or watershed delineation and characteristics estimation, surface flow-path mapping, and stream network extraction [16,17]. DEM data are derived from remote sensing data collected by the National Aeronautics and Space Administration (NASA) missions under the Shuttle Radar Topographic Mission (SRTM) program, which provides near-global topographic coverage of the earth's surface with unprecedented consistency and accuracy [18].

This study aimed to evaluate the system evolution, renewability, and sustainability of the halite harvesting process from the inland sabkha, Al-Qasab-Shaqra, Central Saudi Arabia. The findings will advance the area's inclusion in a long-term industrial plan for utilizing the harvested halite to produce higher-value chemicals through electrolysis. Many approaches are integrated, conceptually and quantitively, based on the following sequence:

1. Delineating the source and origin of water in the study area (renewability) has been partially fulfilled through remote sensing data (SRTM-DEM) processing.

2. Supporting the information gathered from step one through the hydrochemical investigation of the interrelationships among the rainwater chemical composition with those of the source well and solar evaporation ponds.
3. Employing thermodynamic geochemical modelling to identify the precipitation tendency and sequence of the different mineral assemblages.
4. Proposing an improved design for the solar evaporation ponds and their operation to provide a ready feed (i.e., needs no or minimal pretreatment stages) to the electrolysis process, not to the halite harvesting process itself, i.e., devising a new design that is anticipated to fulfil the aims.

1.2. Description of the Al-Qasab Site and the Salt Harvesting Folkloric Process

Al-Qasab is a village located in Shaqra Governorate within the Riyadh region in Saudi Arabia. Al-Qasab is approximately 35 km from Shaqra Governorate and 150 km northwest of Riyadh's capital. It is one of the largest towns in the Al-Washm region and is administratively affiliated with Shaqra Governorate. Al-Qasab is located at the end of Al-Hamada which is a wide, plain land extending from Dharmaa to Al-Hareeq in the heart of the Arabian Peninsula, northwest of Riyadh, in the central region of the Kingdom of Saudi Arabia. It is famous for producing salt (table salt) extracted from the ground, producing more than a third of the Kingdom's need for coarse salt. The Al-Qassab land is plain, as it is hard to see anything above the surface except for a few ridges adjacent to the dry valleys descending from the Tuwaiq Mountains. As such, many streams follow the direction of the slope, forming valleys or wadis of reeds that descend from the Tuwaiq Heights in the northeast, and all of them drain into a southern part. Among these valleys or wadis are (a) Al-Batin is in the west, where Al-Qasab is located on its eastern edge, and it descends from the north and northeast; (b) Shuaib Abtalhat, located to the west of Aba Al-Jarfan. Moreover, many other valleys are widespread in the area, all crossed by the Huraimla Al Qasab Road from Riyadh.

The Al-Qasab playa (i.e., sodium chloride salt solar evaporation and harvesting operational ponds) is located west of Mount Tuwaiq, southeast of the new city of Al-Qasab, approximately five kilometers east of the road to Tharmada. It extends from east–northeast to west–southwest at an orientation angle of 63 degrees east, with the longest axis reaching 11 km and the largest vertical width reaching 5 km. Therefore, it tends more toward a rectangular than a circular shape, with a shape index of 0.37. The Playa (also called locally Al-Mamlha or Al-Jafara) extends between between E 45°31′19″ and 45°35′0″ and N 25°13′0″ and 25°16′32″ in the northern hemisphere WGS84/UTM zone 37N., as shown in Figure S1. The folkloric salt producers thought that the playa had been a lake of water in the past, and its water dried up due to the recent drought with meager precipitation rates. Its land became a salt marsh. Because water comes to it from all sides and does not come out of it (i.e., closed basin), the soluble salts are heavily concentrated as the water evaporates. The water drains from the edge of Mount Tuwaiq and the upper Ariq al-Buldan, flowing towards the saltwater through clear valleys or low parts between the dunes in the Ariq al-Buldan. It has been mentioned in the famous heritage book Al-Isfahani, 1968, p. 273, that the valleys of al-Ragham (the dunes located east of Al-Washm and called the Ariq al-Buldan) lead with their water to the Arramadah playa, which is a salt marsh near the Al-Qassabah, which is now the Al-Qasab. As such, the role of Ariq Al-Buldan, with its various dunes, in supplying the Al-Qasab salt mill with water since ancient times is indicated. The breadth of Ariq Al-Buldan is 6.9 km, and it approaches the southwestern end of the salt pan. They are 1–2 km apart, and this aspect, with its height and the porosity of its sandy deposits, with an average slope of 3.5 degrees, plays a crucial role in draining water towards the Al-Qasab playa. Some small dunes, Al-Faydat and Al-Rawdat, near the Playa's western side, form low-lying areas. The Al-Faydat represents the mouths of wadis and Al-Shuaibs (i.e., tiny wadis), taking a longitudinal shape. The water from the Al-Faydat overflow reflects the poor drainage, representing the estuary area of Wadi Al-Maqrah directly northwest of Al-Qasab Playa. According to the oral narrations repeated among the

people of Al-Qasab, it is ancient from time immemorial, and it was in an area closer to the current town of Al-Qasab than its current location on the course of the Al-Batin Wadi from the east. The immigration to the current location began in the late Hijria seventies or the Christian seventh century. Since then, salt has been the main product of the inland sabkha, supplying cities and villages throughout the Kingdom of Saudi Arabia and even exported to Yemen and some other Arab Gulf states. Several factories were established in Al-Qasab to pack the harvested, dried salt in different sizes for domestic use and export.

The ancient inhabitants developed a folkloric salt harvesting process, which has been adopted until now with some modifications to use suitable motor-operated machines, pumps, and cranes whenever possible. It goes through the following consecutive steps:

a. The salt producer digs a spring or a well called Ain Al-Jafr (i.e., the local name in Arabic, which means the mouth or hole of the salt mine).
b. A large clay reservoir called a tank is made adjacent to Ain Al-Jafr. This reservoir shall be slightly above ground level to allow the salt water to flow into the next ponds.
c. Medium-depth ponds of different lengths are excavated next to the reservoir.
d. Water is pumped from the well or spring (Ain Al-Jafr) using pumps to fill the main reservoir or tank.
e. The ponds are filled consecutively from the tank, which is concentrated by solar evaporation until the salt solubility limit is reached and deposited on the pond's surface, forming a thick layer of white salt. This concentration process spans two to four months depending on the climate conditions, especially air temperature and the intensity of the wind.

The crystallized salt is washed and collected in piles for solar drying before packing. The whole process is depicted in Figure 1.

Figure 1. Folkloric salt harvesting process from Al-Qasab Playa, Shaqra, Saudi Arabia.

2. Materials and Methods

2.1. Sampling, Preservation, and Wet-Chemistry Analyses

Water samples were collected from a source water well pumping enough water to reflect the well's water geochemistry. The samples from the subsequent solar evaporation ponds were collected after gently mixing the pond's water in the middle of its longest side. Polypropylene plastic bottles of 1 L capacity were used and thoroughly rinsed with the sampled water several times before being filled, preserved, and cooled according to the analytes' relevant sampling and preservation best practices guidelines. All wet chemistry analyses were carried out at the Water and Environment Research Unit (WERU) College of Science and Humanities at Ad-Dawadmi, Shaqra University laboratory, where samples were split, pretreated, and acidified to pH < 2 according to the relevant standard method and sampling rules [19–21]. The study area location map and the folkloric halite harvesting ponds are shown in Figure 2. The electrical conductivity (EC) and pH were measured using an electrical conductivity meter ThermoScientific (Waltham, MA, USA) (ORION STAR A122) and PascoScientific pH electrode connected to an Explorer GLX, Pasco data logger via PASPort CHEMISTRY Sensor (PascoScientific, Roseville, CA, USA), respectively. All hydrochemical analyses were conducted following the Standard Methods for Examining Water and Wastewater procedures [22]. Nitrate (NO_3^-) ion concentration was determined spectrophotometrically at 410 nm wavelength following the modified phenol sulphonic acid method [23,24]. Dissolved organic carbon (DOC) was estimated spectrophotometrically at 254 nm and 275 nm wavelengths employing potassium hydrogen phthalate (PHP) as a proxy, with R^2 values higher than 0.99.

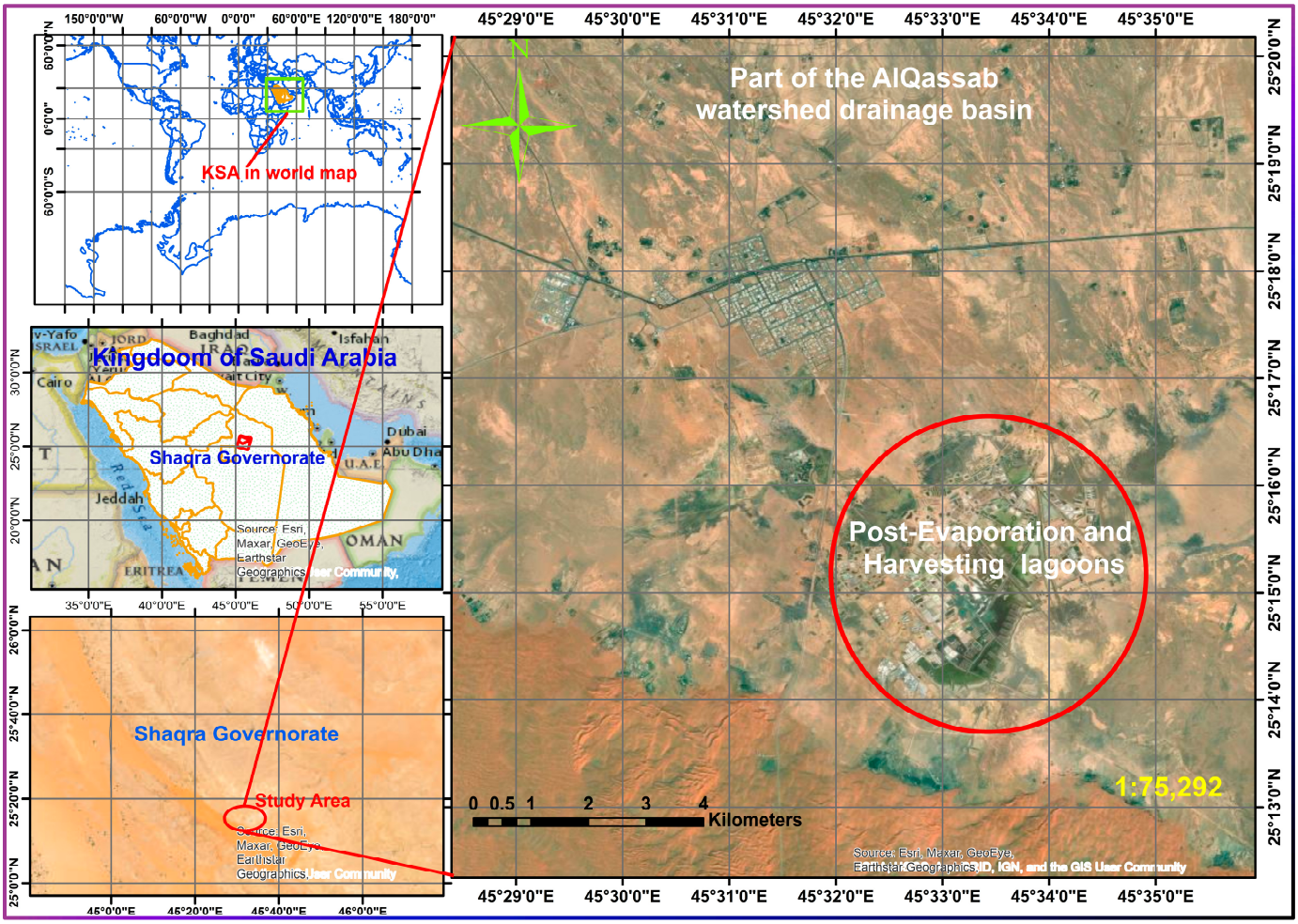

Figure 2. The Al-Qasab Playa and watershed location map.

2.2. Watershed Delineation

SRTM-DEM was invoked and processed using the ArcGIS 10.8 software hydrology ArcTool box tools to interpolate and extract the watershed basin in the region.

2.3. Hydrogeochemical Analysis

Piper, Schoeller, Ludwig–Langelier, Durov, scatter plots, and geochemical plots were constructed using AquaChem®10 (a widely used Water Quality Data Analysis and Reporting Software) to classify, analyze, plot, and report hydrogeochemical data.

3. Results and Discussion

3.1. Delineation of the Watershed Drainage Basin

Morphometric analysis is a quantitative measurement and mathematical analysis of various parameters, such as elevation, slope, and other attributes that define the land surface and forms' shape and topographic configuration. Recently, processing the remote sensing data (DEM) using ArcGIS tools has been commonly used to delineate drainage morphometric characteristics, which are essential for understanding the geohydrological characteristics of a drainage basin concerning the terrain feature and its flow patterns and providing quantitative insights into the formation of streams, their ordering, and the development of basins. The morphometric study of a basin provides valuable information about its drainage characteristics, including areal aspects (basin area, drainage density, basin shape, circulatory ratio, etc.), linear aspects (basin length, stream order, steam length, mean stream length, etc.), and relief aspects (basin slope, gradient ratio, basin relief, etc.) of a watershed, and this information is computed to derive the general character of the watershed. Recently, with the advancement of remote sensing and spatial technology, the computation of various terrain and hydro-morphometric characters of drainage basins was simplified [16,25–28]. The digital elevation map (DEM) for the Al-Qasab region was downloaded from the Earth Explorer website from NASA's Shuttle Radar Topography Mission (SRTM) dataset with a resolution of 30 m [18]. The watershed was delineated using this DEM-SRTM dataset employing the tools included in the Hydrology Arctoolbox module in the ArcGis V10.8 (Figure 3). The slope and relative elevation parameters are believed to influence and control recharge to the playa watershed. The harvesting solar evaporation ponds collectively lie within an area of ≈30 km^2. The center of the watershed drainage is 639 m above mean sea level (amsl), with the surrounding areas reaching 931 m amsl from the west and northern east sides. The Al-Qasab surface is primarily plain, and its morphology generally slopes towards the south. The Al Mu'asibah and Ad Dahinah in the northern east and Ushaiqer, Shaqra, Uthaithiah and Al Ghurabah in the west are the highest at 840 to 931 m amsl, and the Al-Qasab Village and Al-Qasab salt flats in the southeast are the lowest lying plains at 627 m amsl as evident in Figure 3. The extracted information indicates that the Al-Qasab watershed is a nonmarine closed basin with a drainage watershed area of 1290 km^2, which is considerably large enough to secure a long-term supply of salt, as confirmed through its continuous operation from the Christian seventh century until now. The vectorized representation of the morphometric surface elevation map demarcates the water flows toward the southeast part, which is the current salt production area.

3.2. Descriptive Statistics of the Physicochemical Data

The descriptive statistics of the physicochemical data of the collected water samples from an operational consecutive solar evaporation pond starting from the source well to the final harvesting pond are given in Table 1. Along with the descriptive statistics, the results of the Anderson–Darling normality test are supplied with their *p*-values. If the *p*-value is less than the significance level (α), the decision is to reject the null hypothesis (Reject H_0) and conclude that the data do not follow a normal distribution. Otherwise, when the *p*-value is equal to or larger than α, the decision is that the data do not follow a normal distribution, i.e., fail to reject the null hypothesis (Fail to reject H_0). More accurately,

insufficient evidence is available to conclude the data follow a normal distribution. The pH ranged from 6.82 to 7.92 with a mean of 7.54 and standard deviation (SD) ± 0.249 (n = 12), i.e., the water in the solar evaporation ponds ranged from semi-neutral (6.82) for the source to slightly alkaline with progressive evaporation. The pH data are left-skewed with a skewness value of −1.65, i.e., the distribution tail points to the left with the pH propagates going from the source to successive solar evaporation ponds. This trend may point to crystallizing, separating, or complexing of the acidic ions with the progression of the evaporative concentration process. Such an increasing trend in pH was supported by the Anderson–Darling normality test, as the results failed to reject H_0 because it decreased again at the third solar evaporation pond (i.e., following semi-unidirectional change) with a positive Kurtosis value (2.63), indicating that the data are distributed with heavier tails than observed in a normal distribution. Moreover, this positive Kurtosis value suggests that the pH statistically follows the student's t distribution as it had a lower value (6.82) for the source well, reached the maximum (7.92) in pond 2 and decreased again (7.81) in pond 3, forming a bell-shaped variation starting from the source well to pond 3.

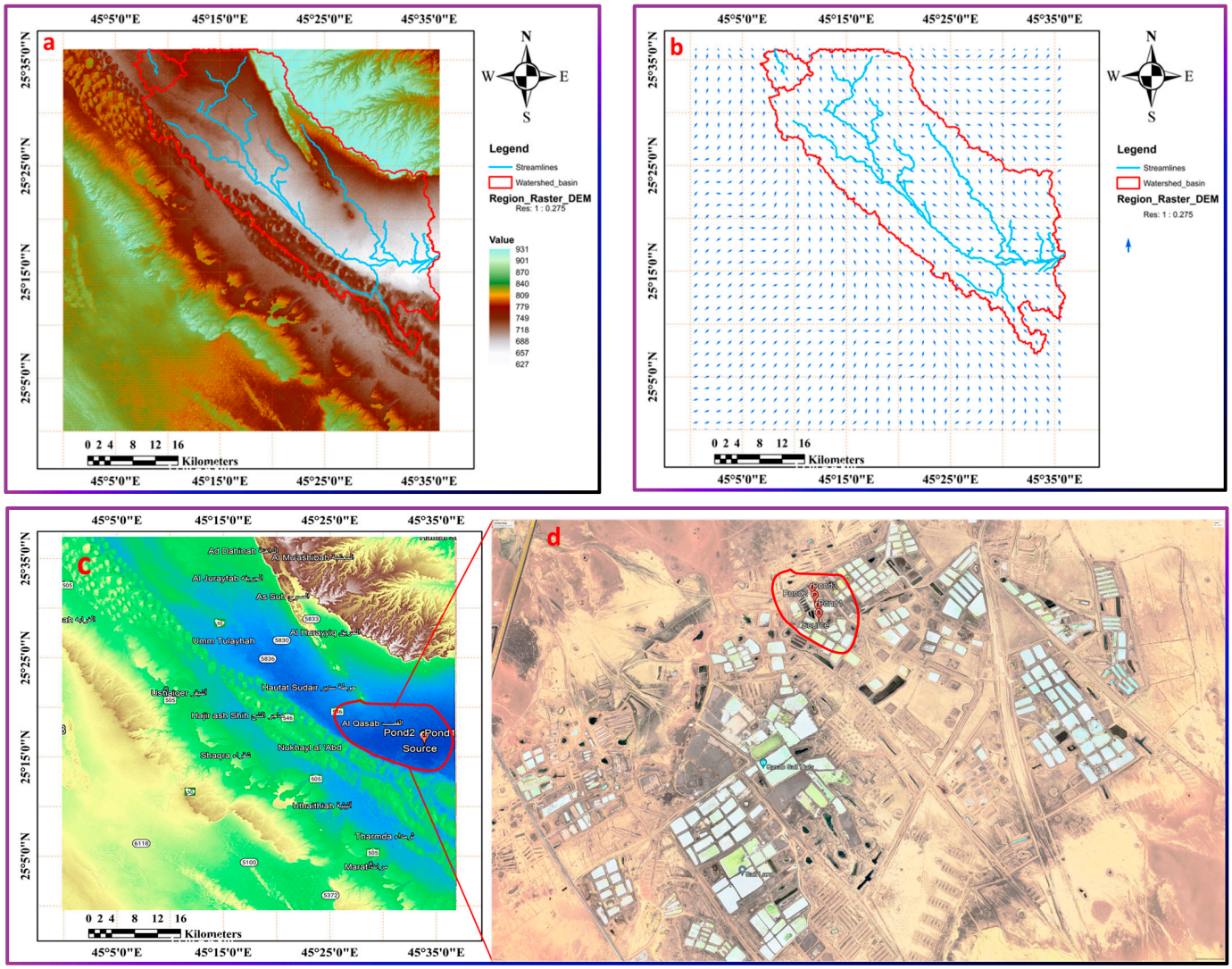

Figure 3. The morphometric surface elevation map (**a**), its vectorized representation (**b**), and the areal shoot of the folkloric halite harvesting ponds (**c**,**d**) in the Al-Qasab region, Central Saudi Arabia.

Table 1. Descriptive statistical summary of the measured and collected physico-chemical properties.

Variable	Mean	SE Mean	StDev	Minimum	Q1	Median	Q3	Maximum	Range	IQR	Skewness	Kurtosis	Anderson–Darling Normality Test	
													p-Value	Decision
Na (ppm)	105,303	14,250	28,500	67,260	76,320	109,460	130,130	135,033	67,773	53,810	−0.80	1.08	0.64	Fail to Rej. H_0
Na (epm)	4578	620	1239	2924	3318	4759	5658	5871	2947	2340	−0.80	1.08	0.64	Fail to Rej. H_0
K (ppm)	4718	699	1398	3100	3325	4941	5888	5890	2790	2563	−0.35	−4.03	0.212	Fail to Rej. H_0
K (epm)	121.0	17.9	35.8	79.5	85.3	126.7	151.0	151.0	71.5	65.7	−0.35	−4.03	0.212	Fail to Rej. H_0
Ca (ppm)	9023	3424	6848	1	2006	10,025	15,038	16,040	16,039	13,032	−0.75	0.34	0.705	Fail to Rej. H_0
Caepm	451	171	342	0	100	501	752	802	802	652	−0.75	0.34	0.705	Fail to Rej. H_0
Mg (ppm)	2433	993	1986	1	609	2433	4258	4866	4865	3649	0.00	1.50	0.41	Fail to Rej. H_0
Mgepm	202.8	82.8	165.5	0.1	50.8	202.8	354.8	405.5	405.4	304.1	0.00	1.50	0.41	Fail to Rej. H_0
TC (ppm)	121,477	13,904	27,808	80,813	92,181	132,661	139,590	139,775	58,962	47,409	−1.72	2.90	0.081	Fail to Rej. H_0
TC (epm)	5352	592	1183	3607	4119	5815	6123	6173	2566	2004	−1.81	3.34	0.075	Fail to Rej. H_0
HCO_3 (ppm)	6833	1869	3738	3904	3904	5857	10,738	11,714	7810	6834	0.85	−1.29	0.255	Fail to Rej. H_0
HCO_3 (epm)	112.0	30.6	61.3	64.0	64.0	96.0	176.0	192.0	128.0	112.0	0.85	−1.29	0.255	Fail to Rej. H_0
Cl (ppm)	167,941	16,865	33,730	118,198	133,024	180,527	190,271	192,510	74,312	57,248	−1.80	3.38	0.079	Fail to Rej. H_0
Cl (epm)	4731	475	950	3330	3747	5085	5360	5423	2093	1613	−1.80	3.38	0.079	Fail to Rej. H_0
SO_4 (ppm)	10,719	4530	9061	1375	3219	9188	19,750	23,125	21,750	16,531	0.97	1.99	0.356	Fail to Rej. H_0
SO_4 (epm)	111.7	47.2	94.4	14.3	33.5	95.7	205.7	240.9	226.6	172.2	0.97	1.99	0.356	Fail to Rej. H_0
NO_3 (ppm)	6067	3799	7597	558	665	3414	14121	16,881	16,323	13,456	1.47	1.77	0.166	Fail to Rej. H_0
NO_3 (epm)	97.8	61.3	122.5	9.0	10.7	55.1	227.8	272.3	263.3	217.0	1.47	1.77	0.166	Fail to Rej. H_0
TA (ppm)	191,559	21,670	43,341	129,318	145,643	207,572	221,462	221,774	92,456	75,819	−1.55	2.13	0.13	Fail to Rej. H_0
TA (epm)	5164	567	1135	3516	3967	5577	5947	5985	2468	1980	−1.65	2.63	0.13	Fail to Rej. H_0
ICB	1.765	0.735	1.471	−0.090	0.249	2.040	3.006	3.071	3.161	2.757	−0.66	−2.09	0.424	Fail to Rej. H_0
EC, microS/cm	535,650	60,558	121,117	354,900	411,425	588,400	607,125	610,900	256,000	195,700	−1.94	3.79	0.029	Reject H_0
TDS (ppm)	322,625	35,366	70,731	217,100	250,150	353,100	364,625	367,200	150,100	114,475	−1.94	3.79	0.03	Reject H_0
pH	7.542	0.249	0.497	6.820	7.020	7.715	7.892	7.920	1.100	0.872	−1.65	2.73	0.149	Fail to Rej. H_0
Density(gm/cm^3)	1.255	0.0323	0.0645	1.160	11,875	128	1.2975	1.3	0.140	0.110	−1.78	3.22	0.084	Fail to Rej. H_0
DOCPPM	128.7	56.8	113.7	0.0	19.0	128.6	238.6	257.7	257.7	219.6	0.0044	−2.19	0.783	Fail to Rej. H_0

Total number of samples: 12; *p*-value $\leq \alpha$: the data do not follow a normal distribution (Reject H_0) if the *p*-value is less than or equal to the significance level; *p*-value > α: cannot conclude that the data do not follow a normal distribution (Fail to reject H_0) if the *p*-value is larger than the significance level.

Electrical conductivities (ECs) and total dissolved solids (TDSs), were quantified following the standard method of drying and gravimetric analysis and spanned from over 354,900 to 610,900 µS/cm and 217,100 to 367,200 mg/L, showing a similar divergence ranges of 256,000 µS/cm and 150,100 mg/L, respectively. The relationships between EC and TDS vary between 0.586 and 0.611 from the minimum, maximum, and range, demarcating the occurrence of relative chemical compositional changes as some constituents do not share the EC components, such as dissolved organic carbon (DOC), whereas the TDS components are present in all constituents. Moreover, some ions have lower mobility and, hence, a smaller share in EC, especially in the case of highly concentrated solutions. So, the ratio was 0.611 for the source, decreased to 0.599 for pond 2, and increased again to 0.601 for pond 3 as calcium and magnesium ions and DOC were removed between pond 2 and pond 3. EC and TDS showed the same skewness (−1.94), kurtosis (3.79), and *p*-value for the Anderson–Darling normality test (0.03), with the null hypothesis rejected as expected because the values exhibit unidirectional increase proportional with the evaporation extent. Moreover, to obtain quantitative insight into the changes in EC and TDS from one pond to the next, polynomial and linear regressions were performed against the pond number with the well water source considered pond number 1. Moreover, their trends followed the polynomial regression with Equations (1) and (2) for EC and TDS, respectively.

$$y = -52{,}750x^2 + 342{,}030x + 76{,}200,\ R^2 = 0.9491 \quad (1)$$

$$y = -30{,}475x^2 + 198{,}165x + 55{,}775,\ R^2 = 0.946 \quad (2)$$

The regression equation variables y and x refer to EC or TDS, and the pond number with the source well water was considered pond number 1 (in this regression only). The regression coefficient for linear regression was 0.696 due to the slower rate of concentration change at ponds 2 and 3 following a semi-plateau. Such a trend may be ascribed to both the precipitation of some constituents reaching their solubility limits as the evaporative concentration process proceeds and the negative effect of concentration on the vaporization tendency according to Raoult's law. The ionic charge balance equilibrium (ICBE) among total anions (T_Z^-) and total cations (T_Z^+) ranged from −0.07 to +3.07, with a mean and median of +2.046 and +1.76, respectively, and SD ± 1.47. Despite the skewness and Kurtosis value being slightly shifted to the negative tail, they revealed that the chemical analysis was statistically controlled, providing fit-for-purpose reliability in the analysis results and the afterwards drawn data.

The Na^+ and K^+ cations range from 67,260 to 135,033 and 3100 to 5890 mg/L, respectively, from the source to pond 3, confirming successful evaporative concentration. Meanwhile, the Ca^{2+} and Mg^{2+} cations showed a different pattern as they increased from the source at 8020 and 2433 mg/L, respectively, reaching the maximum values of 16,040 and 4866 in pond 2, and finally dropping below the detection limit in pond 3. The Cl^- and SO_4^{2-} followed an increasing trend from the source to pond 3 with minimum values of 118,198 and 1375 mg/L in the source water and maximum values of 192,510 and 23,125 mg/L in pond 3, respectively. Meanwhile, the HCO_3^- followed a trend similar to Ca^{2+} and Mg^{2+} cations, increasing from 3905 in the source to a maximum value of 11,714 in pond 2, and dropping again to 3904 in pond 3. Such a trend may be ascribed to the coprecipitation when reaching the solubility limits, as discussed in the upcoming section regarding geochemical modelling. Although NO_3^- showed an exceptionally high concentration level, it followed no specific trend from the source to the solar evaporation ponds. The constituents showed a continuous concentration trend, changing over a wide range (higher CF, where CF is the concentration factor for each step calculated as the constituent concentration in the current pond over the constituent concentration in the preceding one) from the source to pond 1 and exhibited a far lower CF thereafter. In the box plot for the constituents shown in Figure 4a, most constituents are generally not normally distributed, confirming the effect of solar evaporative concentration as an accumulation process, especially in pond 1 for all constituents.

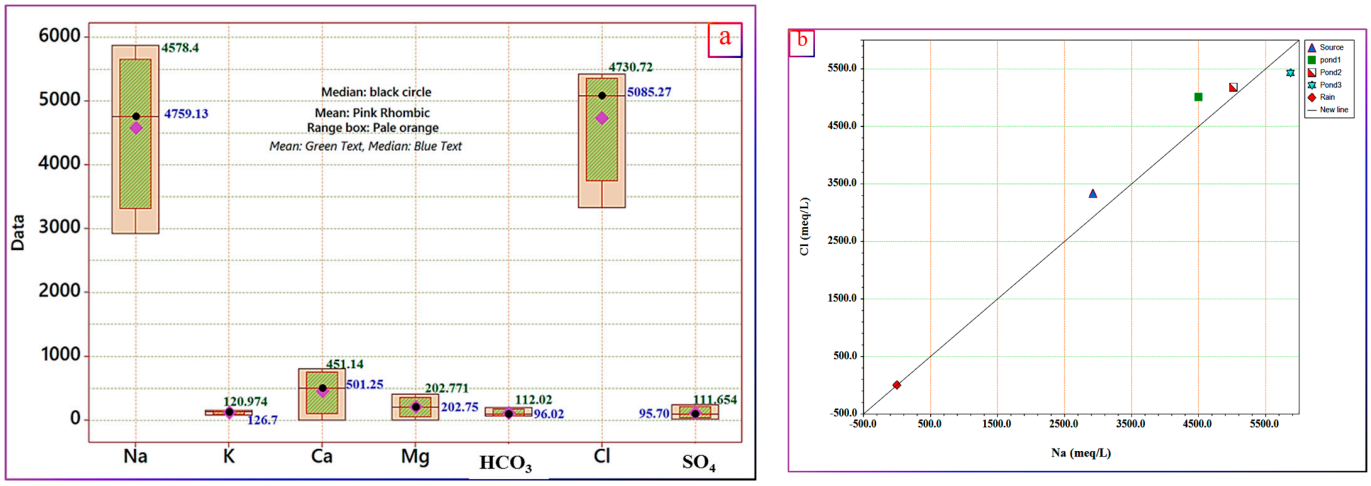

Figure 4. Box plot of the constituents in the source and evaporative concentration ponds, in mEq/L (**a**) and the ionic relationship between Na^+ and Cl^- expressed in mEq/L (**b**).

A significant shift between the mean and median statistics is noted for Na^+ and Cl^-, with Cl^- exhibiting the more intense shift. This shift may be attributed to the precipitation of Cl^- in proportions larger than that consumed in forming halite (Na/Cl = 1), as confirmed by tracing Cl^- changes with Na^+ in Figure 4b. As apparent in Figure 4b, Cl^- is higher than the 1:1 line in the source, approaches that line in pond 2, and is under the line in pond 3, confirming the consumption of Cl^- in processes other than halite formation.

3.3. Major Constituent Distribution

Na^+, Ca^{2+}, K^+, Cl^-, and $SO_4{}^{2-}$ are the most abundant cations and anions in the source water. The distribution of such constituents with Mg^{2+}, $HCO_3{}^-$, and $NO_3{}^-$ throughout the solar evaporation system from the source water to pond 3 is depicted in radial diagrams and pie plots (Figure 5). The concentrations are expressed in mEq/L units to help visualize the relative equilibrium distributions and changes, indicating a quasi-uniform relative distribution of Na^+ and Cl^-, regardless of the source or pond. However, the Ca^{2+} and Mg^{2+} loads exhibited remarkable variations, with the most abrupt change noted between pond 2 and pond 3. This abrupt change indicated their crystallization and separation from the solution after reaching the maxima in pond 2. The solar evaporation mechanism and contact with air leads to the absorption of atmospheric carbon dioxide, leading to increased contributions of $HCO_3{}^-$, which showed changes consistent with that of Ca^{2+} and Mg^{2+} and precipitation as calcite, dolomite, and the other relevant minerals, as will be discussed in the geochemical modelling section.

3.4. HydroGeochemical Changes Using Geochemical Diagrams

Chadha [29], Piper [30], Durov, and Schoeller scatter plots and Ludwig–Langelier diagrams are exploited in the following section to understand better and facilitate the system's interpretation, particularly evolutionary trends, controlling processes, and hydrogeochemical facies.

a. Chadha Plot

The chemical composition is described as hydrogeochemical facies based on the type of dominant constituents. The difference between weak acidic and strong acidic anions $((HCO_3{}^- + CO_3{}^{2-}) - (SO_4{}^{2-} + Cl^-))$ expressed in mEq/L on the ordinate is plotted against the difference between the alkaline earth and alkali metals $(Ca^{2+} + Mg^{2+}) - (Na^+ + K^+)$ on the abscissa with the same units used in the y-axis. The Chadha plot in Figure 6a reveals that all samples fall under the Na^+-Cl^- subfield. A point representing the average chemical composition of rainwater in the Riyadh region provided by Alabdula'aly and Khan [31] is included to help demarcate the differences between source water and rainwater.

Interestingly, it lies within the subfield, indicating a similar origin. Moreover, linear regression showed a perfect fit in Figure 6b, with a regression coefficient of 0.9947 for the rain, source, pond 1 and pond 2 samples. The pond 3 sample was excluded as it suffered a rigorous abrupt change due to complete precipitation of calcium and magnesium as they reached their solubility limits. This perfect regression confirmed the rain origin of the source water with minimal geogenic alterations, except for the evaporative concentration, as they still fit with pond 1 and pond 2, which were exposed to vigorous solar evaporation.

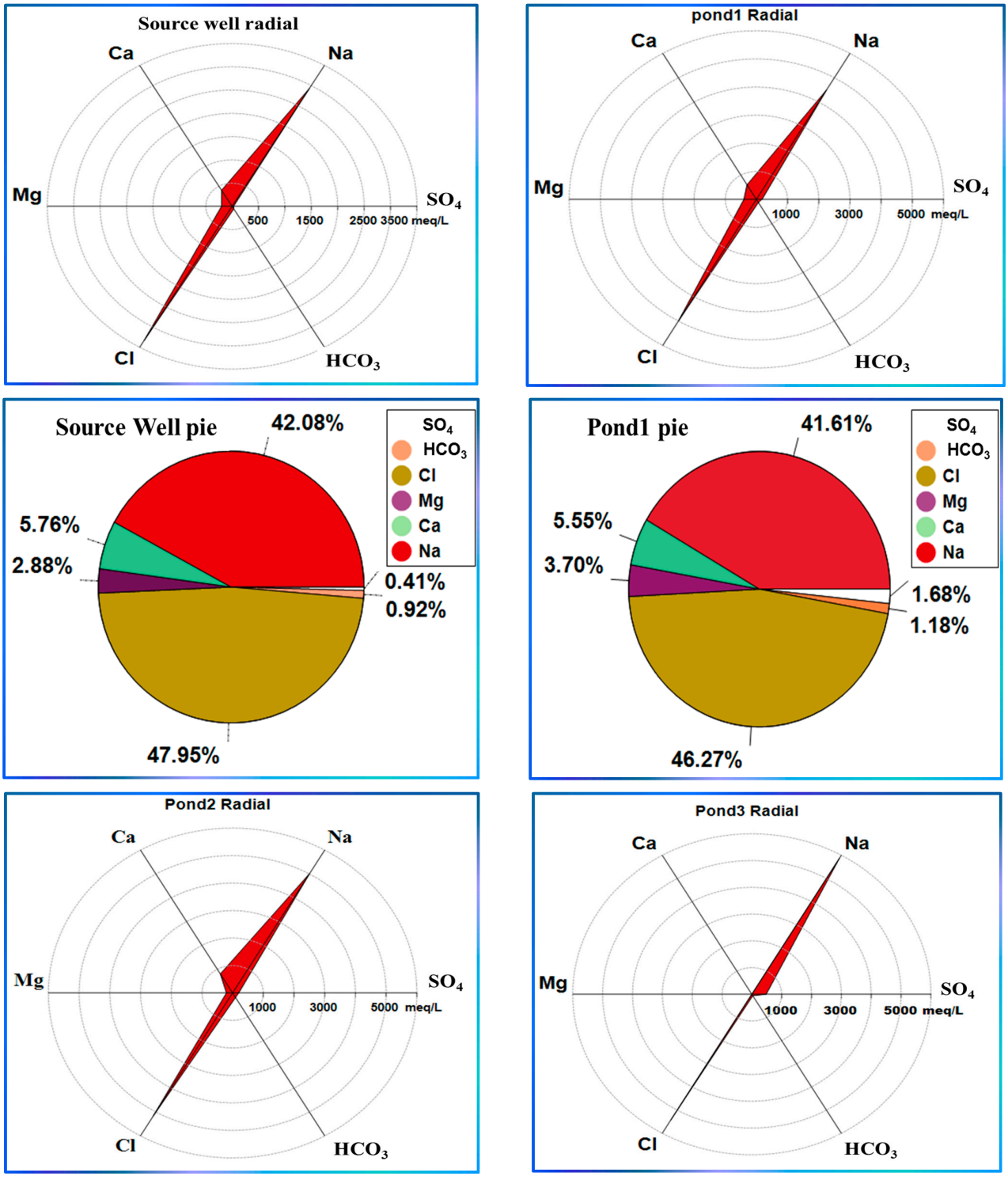

Figure 5. *Cont.*

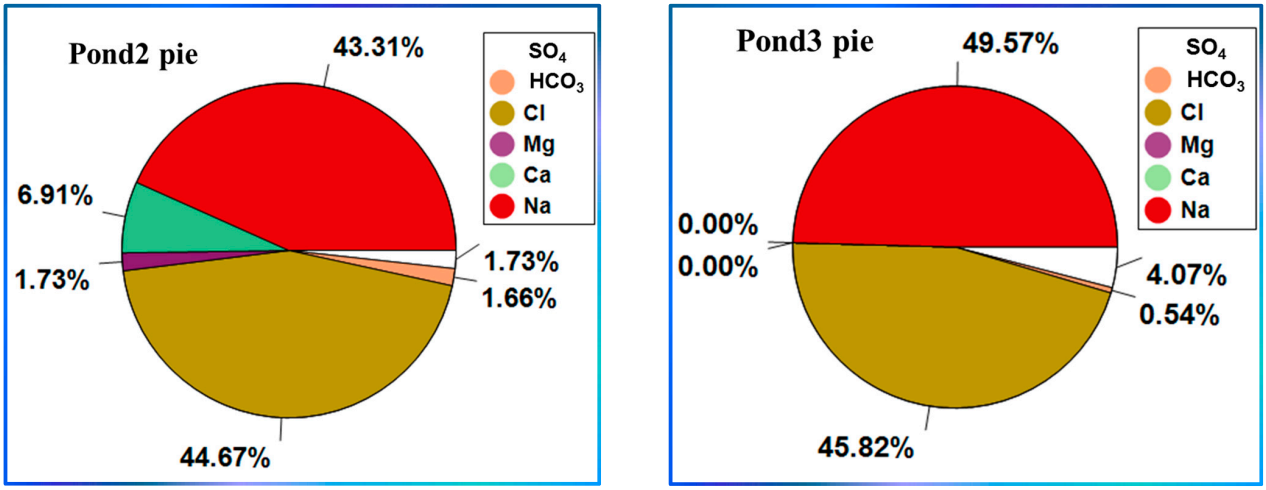

Figure 5. Radial diagrams and pie plots of the cation and anion constituent distributions in the source water and the subsequent solar-driven evaporation ponds.

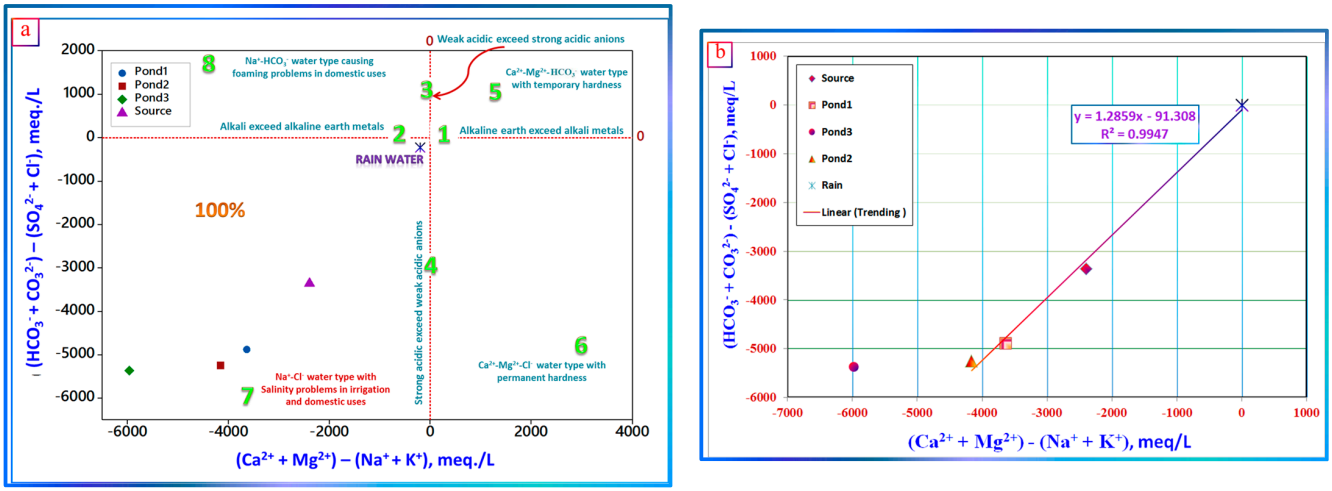

Figure 6. Chadha hydrogeochemical classification (**a**) and its linear regression (**b**).

b. Piper Plot

The widely utilized graphical Piper diagram is composed of two separate trilinear plots together with a central quadrilateral diamond plot on which the relative concentrations of the major anions and cations are portrayed with three data points representing every sample as milliequivalent percentages. The points from the two trilinear plots are projected on the central quadrilateral diamond, showing the overall chemical character and revealing specific properties of the total ion relationships in the water [32]. Although the Piper plot does not depict the absolute ion concentrations with relative percentages like all trilinear plots, it facilitates the visual comparisons of six parameters, enabling the samples' clustering and inferring their hydrogeochemical facies and hence demarcating the origin, chemical evolution, and pathways mixing from different sources and water types according to the ionic composition [32–35].

Only changes in the major constituents' relative proportions are noted, not changes in the total load, as the Piper plot does not portray the absolute ion concentrations. The Piper plot and the classifications within it are shown in Figure 7a. The plot clarified the occurrence of a dramatic evolution of the hydrochemical facies from the rainwater to the source well water, with the rainwater found within the magnesium-bicarbonate water type in the quadrilateral diamond and calcium type and bicarbonate type within the cations and anions triangles, respectively. The source water well and the water in the subsequent

solar evaporation ponds lie in the dominant Na^+/Cl^-, Na^+/K^+, and Cl^- subfields in the quadrilateral diamond, cation triangle, and anion triangle, respectively, according to the classification subfields shown in Figure 7a. The pond 3 sample lies within the same subfield as the other samples but at the outermost fringe, as it experienced an intense evaporative concentration process with precipitation of the other co-occurring Ca^{2+}, Mg^{2+}, and HCO_3^- ions. Although the source water was exposed intentionally to vigorous solar evaporation with no geogenic interactions, the source and pond water samples fall under the Na^+ (K^+) Cl^- (SO_4^{2-}) water type. As shown in the central quadrilateral diamond plot, the pond 3 sample falls in the field of Cl^-–SO_4^{2-} and Na^+–K^+ (saline) of sodium chloride type, i.e., non-carbonate alkali with no Ca^{2+} and Mg^{2+} hardness forming ions. All in all, the samples lie in the Na–Cl subfield facies in the quadrilateral diamond of the Piper diagram, emphasizing the saline nature [36]. The absence of hardness-forming ions in the pond 3 sample is an advantage, eliminating the need for costly and power-consuming steps of softening using ion exchange resins or nanofiltration as it can be used directly as a ready feed for the chlor-alkali process for producing NaOH, Cl_2, and H_2 gases through electrolysis.

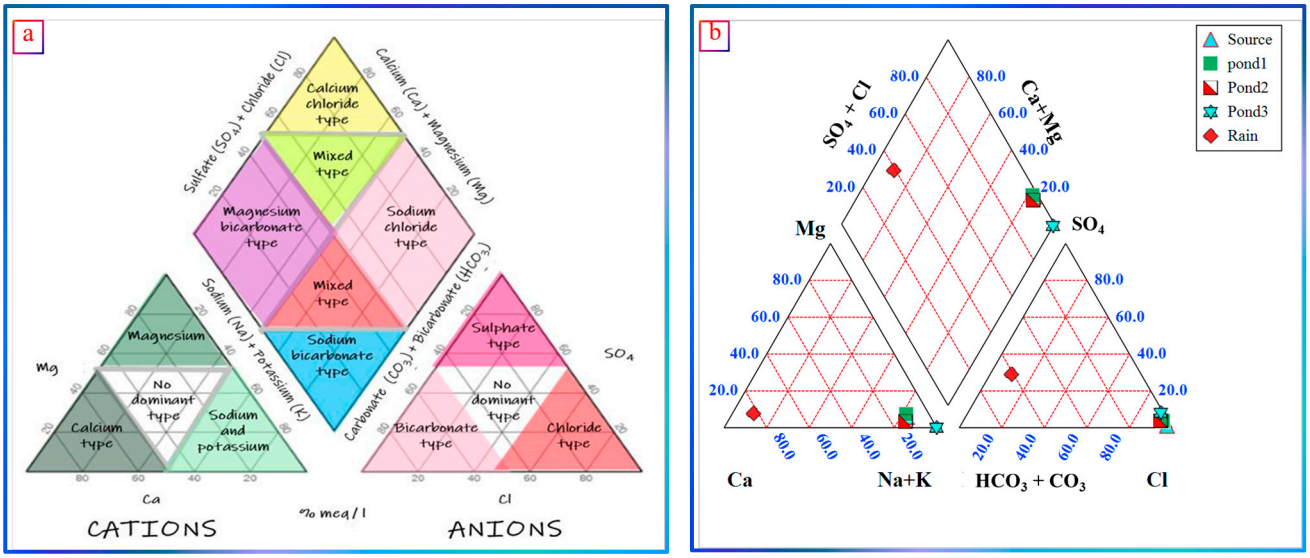

Figure 7. Piper diagram clustering the samples according to their major constituents distribution. (**a**) show the meaning of the plot's different sections; (**b**) samples clustering.

c. Schoeller diagram and Ludwig–Langelier plot

Schoeller's diagram demonstrates the dominance of Na^+ and Cl^- ions with lower SO_4^{2-} and HCO_3^- concentrations than the equivalent levels of Mg^{2+} and Ca^{2+} (Figure 8a). The rainwater samples show a remarkable change in the relative proportions of the constituents as the conservative and semi-conservative ions propagate continuously, while those experiencing different geochemical and hydrochemical patterns of ion exchange or precipitation of the hardness- and lower solubility mineral-forming ions, namely Ca^{2+}, Mg^{2+}, HCO_3^-, and to a lower extent SO_4^{2-}, do not change. Interestingly, source well water and pond 1 and pond 2 samples exhibit a Na^+/Cl^- ratio of less than one, which reversed for pond 3, indicating chloride consumption in crystal-forming phases of calcium and magnesium-based minerals, as will be demonstrated in the geochemical modelling section. The strong acid SO_4^{2-} ion is comparable to the HCO_3^- weak acid except for in the source well water where the HCO_3^- dominates over SO_4^{2-}. This is similar to the patterns noted in rainwater, suggesting the occurrence of congruent concentration for both ions. The alkali metal Na^+ dominates over alkaline earth metals (Ca^{2+} and Mg^{2+}) except for in rainwater. Moreover, Cl^-, SO_4^{2-}, and HCO_3^- levels are higher than Na^+ and Mg^{2+} but lower than Ca^{2+}. The Ludwig–Langelier plot in Figure 8b notes that the sum of Cl^- and

SO_4^{2-} is fourfold the sum of Na^+ and K^+ (i.e., following the regression line of slope equal to four) for the rainwater sample, while the slope for the source water and the ponds samples lie between 1.2 and 1. Such a variation hints at the removal of SO_4^{2-} during its journey from rainwater until it becomes groundwater abstracted through the source well and a proportional concentration of Cl^- and alkali ions.

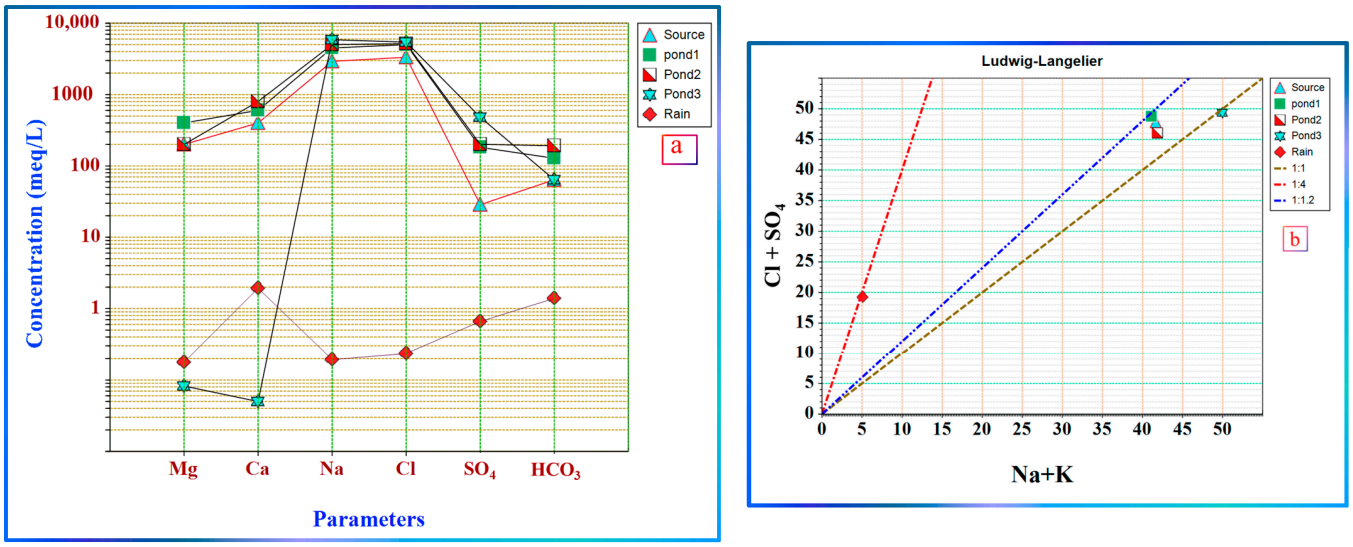

Figure 8. Scholler diagram (**a**) and Ludwig–Langelier plots (**b**) showing the relative major ions distribution.

d. Durov diagram

The Durov diagram in Figure 9 is comparable to Piper's plot, showing identical distributions in addition to TDS and pH representation. It elaborates that the rainwater has slightly alkaline pH values and low salinity levels, with HCO_3^- and Ca^{2+} dominating over other constituents. This rainwater evolved to the source well water with a slightly acidic pH value of 6.82, diminishing the proportions of HCO_3^- and Ca^{2+} in favor of Cl^- and Na^+, respectively. All other samples affected by solar evaporation are distributed within the same subfields in all Durov diagram partitions with slight shifts toward higher salinity and the strongly acidic and alkali metal ions share. This evolution trend suggests that the rainwater might be exposed to mild water–rock interactions and rock weathering combined with concentration evaporation and evaporation-driven precipitation, leading to the evolution of its water composition to that of source water.

e. Gibbs Diagram

Evaporation, mixing, ion exchange, reverse ion exchange, and evaporation-driven precipitation are the main probable processes controlling and modifying hydrogeochemistry. Ion exchange refers to replacing sodium ions in the solid phase (soil or rock) with calcium and magnesium from the liquid phase (water), i.e., calcium and magnesium bound to the solid phase and sodium are solubilized. The reverse process is called reverse ion exchange, which might happen when sodium (of lower valence) liberates calcium and magnesium from the solid due to the higher concentration and, hence, the activity of sodium. The Gibbs plot has been widely exploited as a powerful tool for discriminating among three main processes affecting hydrochemical evolution [37]. The plot is constructed considering that every process, namely evaporation crystallization, rock–water interaction, and precipitation, has a fingerprint and a particular dominant subfield on one or more water constituents, enabling tracings of evolution or variation. The Gibbs diagram is constructed by plotting TDS on the ordinate versus the anions ratio ($Cl^-/(Cl^- + HCO_3^-)$) and the cations ratio ($Na^+/(Na^+ + Ca^{2+})$) on the abscissas (Figure 10). The plot shows that the rainwater sample, as expected, explicitly lies in the precipitation-dominated subfield.

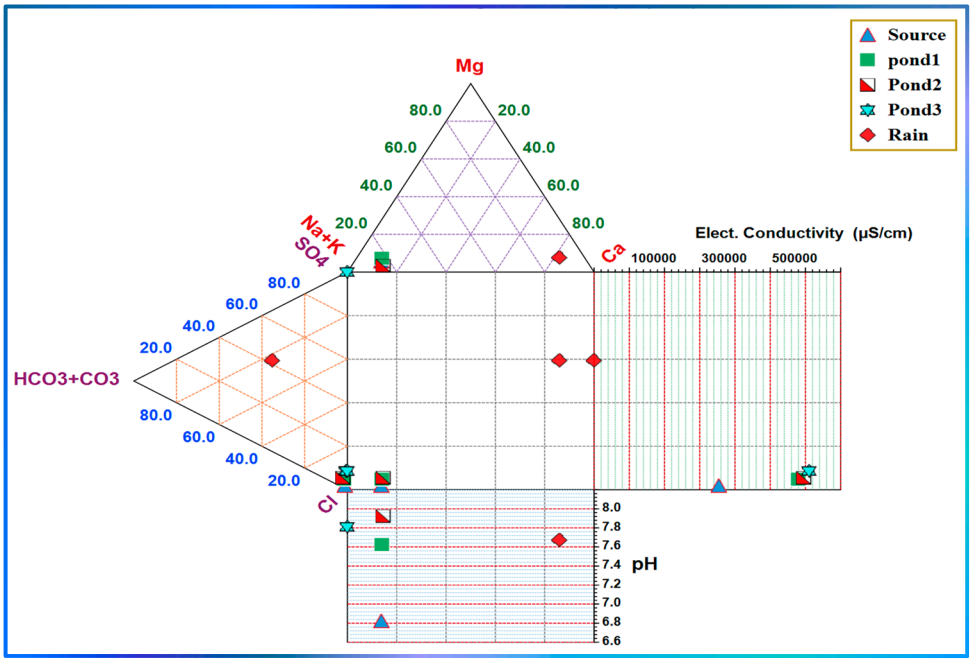

Figure 9. Durov diagram portraying the chemical composition distribution from rain to the solar-driven evaporation ponds.

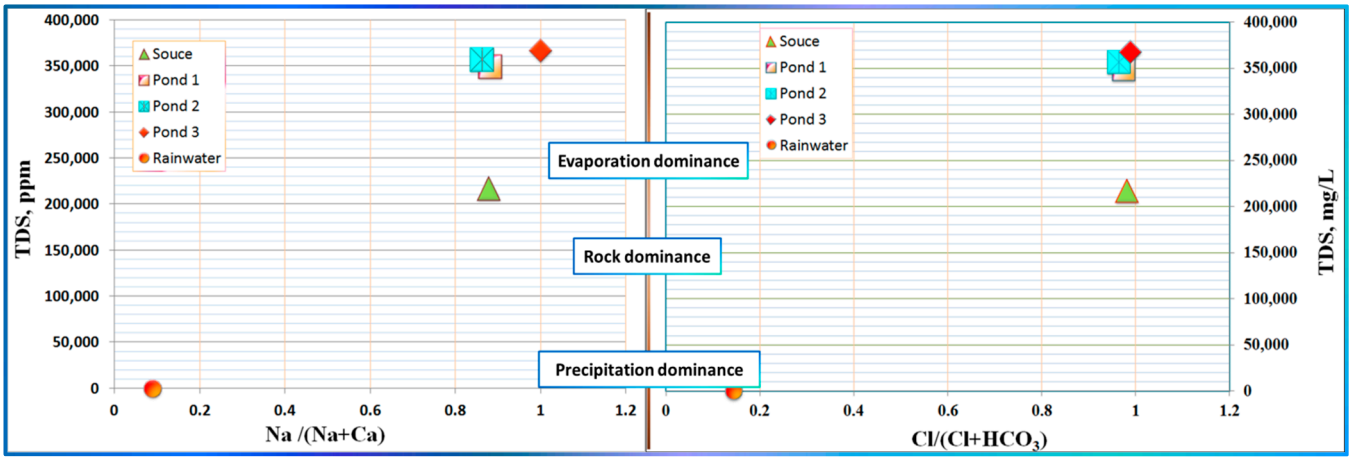

Figure 10. Gibbs plot demarcating the dominance zones of the different water chemistry evolution processes.

Meanwhile, the source well water and samples from ponds 1–3 fall under the evaporation crystallization dominance zone. However, the change in the cation and anion ratios from 0.2 for rainwater to 0.9 and 1 for the source water sample hints at the probable effect of rock weathering, especially silicate weathering, mixing with old hypersaline water, calcite precipitation, and ion exchange on its chemical evolution path. The change from source to pond 3 passes through an upward vertical line as evaporation-driven concentration occurs with slight changes in the cation ratio fringe due to precipitation and removal of calcium. Thus, the Gibbs diagram provides an additional line of evidence of the meteoric precipitation origin of the Playa water. Moreover, it signifies the effect of hyperaridity and hotness (i.e., very high evaporation rates), exacerbating the ionic loads in the infiltrating water flow with other probable salinization processes.

A plot of EC versus the Na/Cl ratio with each expressed in mEq/L is constructed to clarify the effect of evaporation further in Figure S2a. Figure S2a elaborates on the Na/Cl ratio, which slightly changed from 0.823 for rainwater to 0.878 for the source well, while EC

changed significantly from 285 to 354,900 µS/cm for rainwater and source well, respectively. The samples from the solar evaporation ponds showed a remarkable change from 0.9 to 1.08 in the Na/Cl ratio going from pond 1 to pond 3. This result indicates the removal of Cl^- as a counteranion in precipitated minerals, whereas Na^+ was not removed. This theme suggests that the major affecting process is evaporation with a lesser contribution of the rock–water interaction modifying the chemical composition of rainwater, which is, in turn, driven by concentration through intense evaporation. Although Bouwer 1944 pointed out that the Na^+ ion concentration might be enriched over Cl^- from prominent pathways, like leaching of secondary alkaline/saline soil salts, irrigation return flow, and partly by silicate weathering [38], the system under consideration seems to be mainly prone to and driven by the different evaporation processes, including direct solar or capillary rise processes. Plotting (Na^+ and K^+) against total cations in mEq/L ($T_z{}^+$) gave a regression line with a slope of 0.8815 and R^2 value of 0.968, indicating the prevalence of the quasi-conservative nature of the Na^+ and K^+ contribution to the total cations, i.e., no major modifying and/or contribution of other sources to the cation load (Figure S2b).

The contribution of Na^+ and K^+ to the total EC (Figure 11) showed that their contributions follow a power function with powers of 1.30 and 1.02 and R^2 values of 0.999 and 0.998 for Na^+ and K^+, respectively. Ca^{2+} and Mg^{2+} showed different behaviors, exhibiting poor regression for linear and power functions. This theme agrees with the conservative nature of sodium and potassium ions, while calcium and magnesium could be crystallized and separated when reaching their solubility limits. Sodium and potassium ions followed the power regression, suggesting the dominance of Rayleigh distillation or evaporation from ephemeral ponds even for the journey of the rainwater to the source well. In the same way, Cl^-, $HCO_3{}^-$, and $SO_4{}^{2-}$ exhibited similar good power regressions with powers of 1.28, 0.558, and 0.720 and R^2 values of 0.999, 0.954, and 0.889, respectively. Cl^- showed the highest regression parameters, i.e., power and R^2, hinting at its quasi-conservative nature. In contrast, $HCO_3{}^-$ demonstrated a similar good regression despite its non-conservative nature. Such a theme may be attributed to the long-term contact with atmospheric gases, leading to its concentration re-increase when removed through contributions to calcium and magnesium-based minerals. The thermodynamic geochemical modelling results support calcium salt precipitation as aragonite, calcite, dolomite (ordered and disordered), gypsum, and anhydrate because their saturation indices in the source water well (detailed in the next section) are mostly positive. Many other relationships and ion ratios, as shown in Figure 12, corroborate the above inferences that the system is controlled through evaporation with the primary input from precipitation.

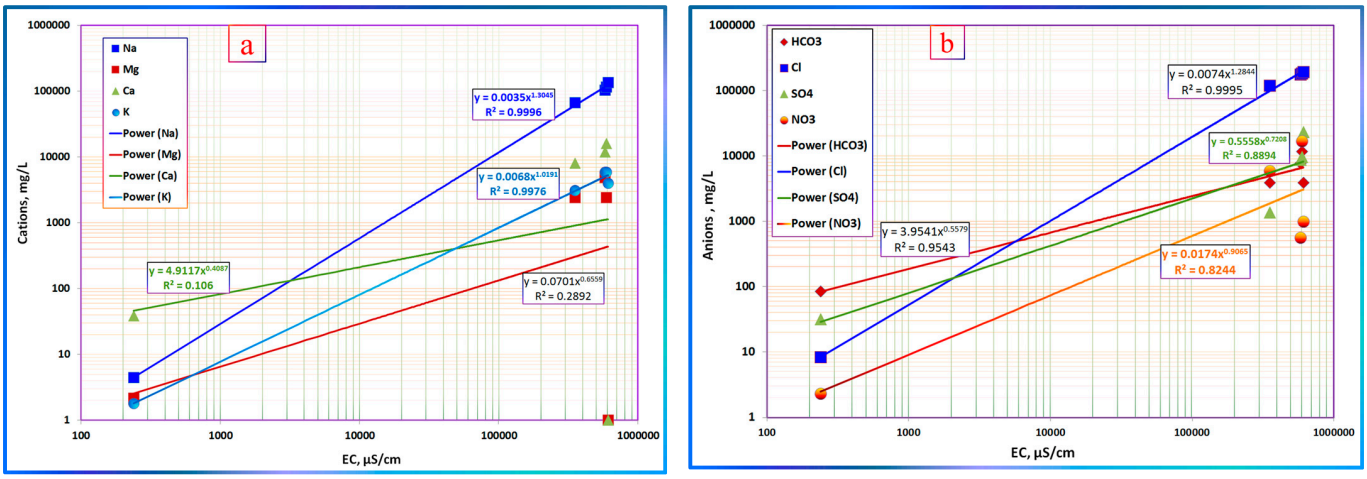

Figure 11. Individual major cations (**a**) and anions (**b**) contributions to the total EC of the GW samples.

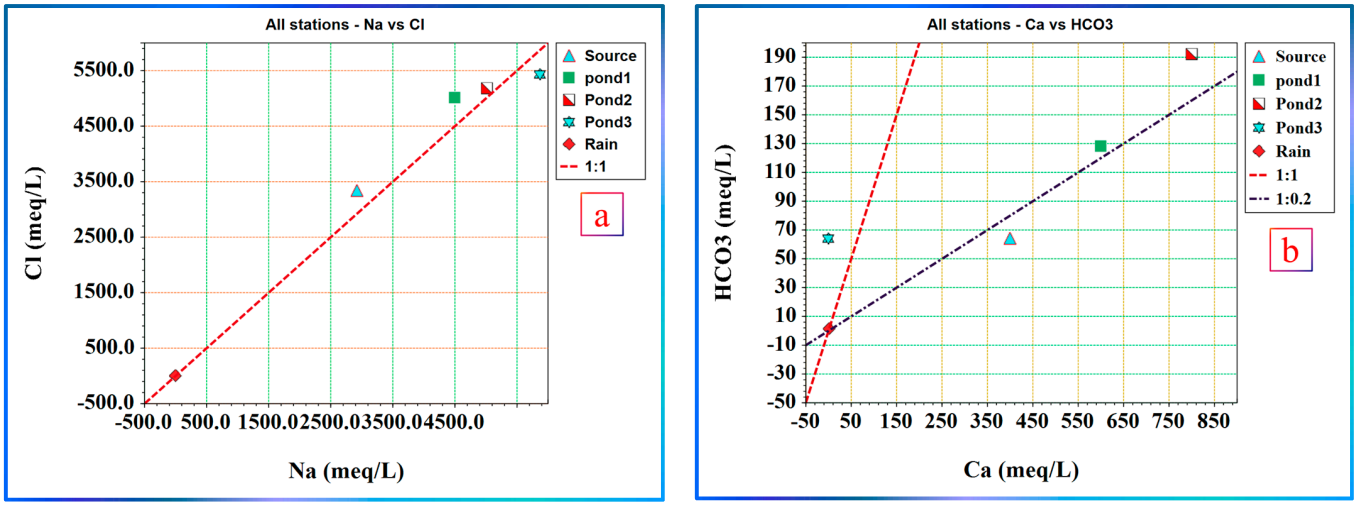

Figure 12. Ionic ratio plots of different combinations among the major constituents.

3.5. Thermodynamic-Based Geochemical Analysis Using PHREEQC Software

This section investigates and determines the mineral assemblages and their salt crystallization sequences in the solar evaporation ponds. This section aims to discriminate the crystallization boundaries of the various minerals in the evaporation ponds and provide mineral clues for the best intake point for the following industrial electrolysis process. The industrial electrolysis process, also known as the chlor-alkali process, is a process that produces caustic soda and chlorine gas in equimolar amounts with electrolysis of aqueous sodium chloride solution. Directly synthesizing process products could produce hydrochloric acid, sodium hypochlorite, or hypochlorous acid. Moreover, hydrogen gas is a coproduct that evolves at the cathode and can be collected and used as a green fuel. Three process variants are in widespread commercial use and are generally distinguished by how the catholyte and anolyte are separated. These variants are known as the membrane, diaphragm, and mercury processes, with the membrane process dominating modern installed capacity because it contains neither mercury nor asbestos-based diaphragms [39,40]. The membrane-based electrolysis process poses requirements concerning the chemical quality and composition of the feedstock, i.e., inlet of the process [41].

PHREEQC (V3.7.3, released December 2012) solubility software [42], an aqueous geochemical thermodynamic-based calculations software, has been used to evaluate which minerals and in which sequence they can crystallize from the solar evaporation ponds. Based on the results of the mineral crystallization sequences, an improved conceptual design of the evaporation ponds, including their number, depth, flow paths, patterns, etc., will be devised in the subsequent section. Moreover, the suitable intake points for the electrolysis will be hinted and commented on. PHREEQC with the Pitzer database for hypersaline solutions was used to calculate the saturation indices (SIs) of the various minerals when the system is considered supersaturated, at equilibrium, or undersaturated when the respective SI is positive, zero, or negative, respectively. The SI values indicate the system's tendency to precipitate or dissolve such minerals and hence their crystallization sequence. The saturation indices of all probable mineral assemblages retrieved by PHREEQC are summarized in Table 2. The SI is calculated as the ion activity product (IAP) divided by the solubility product (K_{sp}), i.e., SI = IAP/Ksp, indicating the respective mineral precipitation. The interpretation of the SIs adopts the following meanings. For values ranging from −1.0 to +0.5, considered imposing no potential dissolution or precipitation at this stage. Rather, this sample is highly likely to precipitation with more concentration (need more evaporation step). For values less than −1.0, the solution is undersaturated. When SI is higher than +0.5, the solution SI oversaturated with a tendency to precipitate. The mineral assemblages show remarkable SIs changes toward the positive fringe going through the cascade from the source well water to the solar evaporation pond 3, as summarized in

the box plot in Figure 13. Most of the minerals showed a lower mean than their median, indicating remarkable variation in their SIs within the intermediate ponds, i.e., pond 1 and pond 2. The area plot, as shown in Figure 14a, provides a clear visualization of the individual changes, with the reference zero line indicating the equilibrium. The areas lying above the line represent those having positive SIs, with the change around this line indicating the readily formed precipitate, as this candidate is likely to precipitate with excess evaporation. Those found far below the equilibrium line are readily soluble with little or no tendency to precipitate until subject to vigorous evaporation or even until complete dryness.

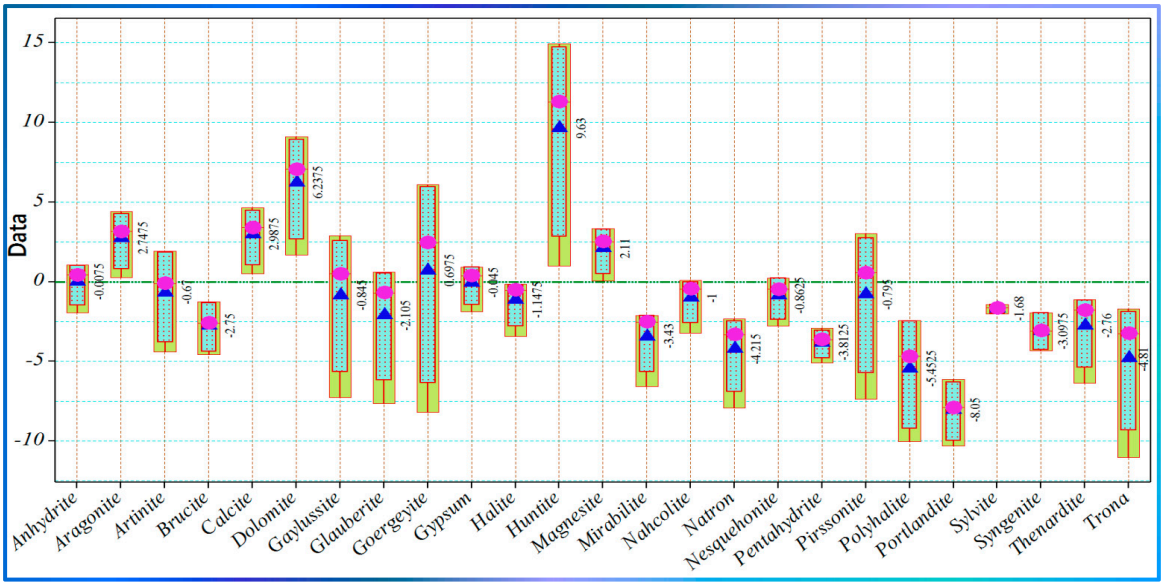

Figure 13. Box plot of the SIs of the considered mineral distributions.

Anhydrite, aragonite, artinite, calcite, dolomite, huntite, gypsum, goergeyite, magnesite, pirssonite, and gaylussite minerals exhibited positive SIs values mostly in pond 1 and pond 2 with calcite, dolomite, huntite, goergeyite, and magnesite demonstrated positive SIs even in the source water, indicating that the system became supersaturated with those minerals as solar evaporation progressed. This concentration-driven evaporation removes the scale-forming minerals early, leaving brine in pond 3, with most minerals having negative SIs. In order to determine which pond has the highest SIs in terms of the number of salts and magnitude, the radar plot was utilized, as shown in Figure 14b. As the radar shows, pond 2 in the current operating pond design has the highest SIs, even for halite. Such a myriad of potential salt precipitation along with halite in one pond could result in admixtures of those minerals rather than pure halite. However, the XRD analysis (Figure 15) of the harvested halite confirmed its purity with only one cubic phase of cubic halite with a unit cell of Cl_4Na_4 and a cell parameter (a) of 0.56423. It is worth noting that two samples collected from different harvesting batches at different times were analyzed and yielded quasi-identical results. The SEM images exhibit the presence of needle-like fibers on the surface of halite crystals. The EDS analysis confirmed the existence of alkali or alkali earth metals other than Na^+. The chemical analysis demonstrated that the Na^+ and Cl^- constituents were present at levels higher than 98%. However, this discrepancy could be attributed to imperfect homogenization issues in the salt sampling during analysis, and the chemical analysis purity index, 98%, is considered the most representative value.

Table 2. SIs for the foremost mineral assemblages.

Mineral Name	Chemical Formula	Saturation Index				Mineral Name	Chemical Formula	Saturation Index			
		Source Well	Pond 1	Pond 2	Pond 3			Source Well	Pond 1	Pond 2	Pond 3
Anhydrite	$CaSO_4$	−0.09	0.94	1.05	−1.93	Kieserite	$MgSO_4 \cdot H_2O$	−4.27	−3.11	−3.54	−5.56
Aragonite	$CaCO_3$	2.52	3.80	4.41	0.26	Labile_S	$Na4Ca(SO_4)_3 \cdot 2H_2O$	−4.59	−1.32	−1.06	−14.36
Arcanite	K_2SO_4	−4.58	−3.43	−3.47	−2.95	Leonhardite	$MgSO_4 \cdot 4H_2O$	−4.23	−3.21	−3.65	−5.43
Artinite	$Mg_2CO_3(OH)_2 \cdot 3H_2O$	−1.89	1.67	1.94	−4.4	Leonite	$K_2Mg(SO_4)_2 \cdot 4H_2O$	−7.38	−5.22	−5.7	−6.96
Bischofite	$MgCl_2 \cdot 6H_2O$	−5.18	−4.3	−3.17	−7.58	Magnesite	$MgCO_3$	1.80	3.25	3.33	0.06
Bloedite	$Na_2Mg(SO_4)_2 \cdot 4H_2O$	−5.53	−3.34	−3.71	−10.73	Mirabilite	$Na_2SO_4 \cdot 10H_2O$	−2.87	−2.16	−2.12	−6.57
Brucite	$Mg(OH)_2$	−3.71	−1.47	−1.26	−4.56	Nahcolite	$NaHCO_3$	−0.58	−0.31	0.1	−3.21
Calcite	$CaCO_3$	2.76	4.04	4.65	0.5	Natron	$Na_2CO_3 \cdot 10H_2O$	−3.79	−2.83	−2.33	−7.91
Carnallite	$KMgCl_3 \cdot 6H_2O$	−6.21	−4.79	−5.14	−8.42	Nesquehonite	$MgCO_3 \cdot 3H_2O$	−1.12	0.20	0.25	−2.78
Dolomite	$CaMg(CO_3)_2$	5.7	8.43	9.12	1.70	Pentahydrite	$MgSO_4 \cdot 5H_2O$	−3.89	−2.92	−3.37	−5.07
Epsomite	$MgSO_4{:}7H_2O$	−3.58	−2.69	−3.17	−4.69	Pirssonite	$Na_2Ca(CO_3)_2 \cdot 2H_2O$	−0.73	1.86	3.04	−7.35
Gaylussite	$CaNa_2(CO_3)_2 \cdot 5H_2O$	−0.73	1.73	2.88	−7.26	Polyhalite	$K_2MgCa_2(SO_4)_4 \cdot 2H_2O$	−6.72	−2.41	−2.65	−10.03
Glauberite	$Na_2Ca(SO_4)_2$	−1.79	0.40	0.6	−7.63	Portlandite	$Ca(OH)_2$	−8.93	−6.86	−6.12	−10.29
Goergeyite	$K_2Ca_5(SO_4)_6 \cdot H_2O$	−0.67	5.57	6.09	−8.20	Schoenite	$K_2Mg(SO_4)_2 \cdot 6H_2O$	−7.16	−5.08	−5.58	−6.67
Gypsum	$CaSO_4 \cdot 2H_2O$	−0.09	0.84	0.94	−1.87	Sylvite	KCl	−2.01	−1.46	−1.43	−1.82
Halite	NaCl	−0.79	−0.23	−0.15	−3.42	Syngenite	$K_2Ca(SO_4)_2 \cdot H_2O$	−4.13	−2.01	−1.94	−4.31
Hexahydrite	$MgSO_4 \cdot 6H_2O$	−3.61	−2.68	−3.15	−4.76	Thenardite	Na_2SO_4	−2.36	−1.20	−1.12	−6.36
Huntite	$CaMg_3(CO_3)_4$	8.47	14.11	14.96	0.98	Trona	$Na_3H(CO_3)_2 \cdot 2H_2O$	−4.05	−2.46	−1.69	−11.04
Kainite	$KMgClSO_4 \cdot 3H_2O$	−5.78	−4.17	−4.59	−6.83	$CO_{2(g)}$	CO_2	−0.43	−1.26	−1.41	−1.29
Kalicinite	$KHCO_3$	−3.12	−2.87	−2.71	−2.94	$H_2O_{(g)}$	H_2O	−1.09	−1.13	−1.14	−1.06

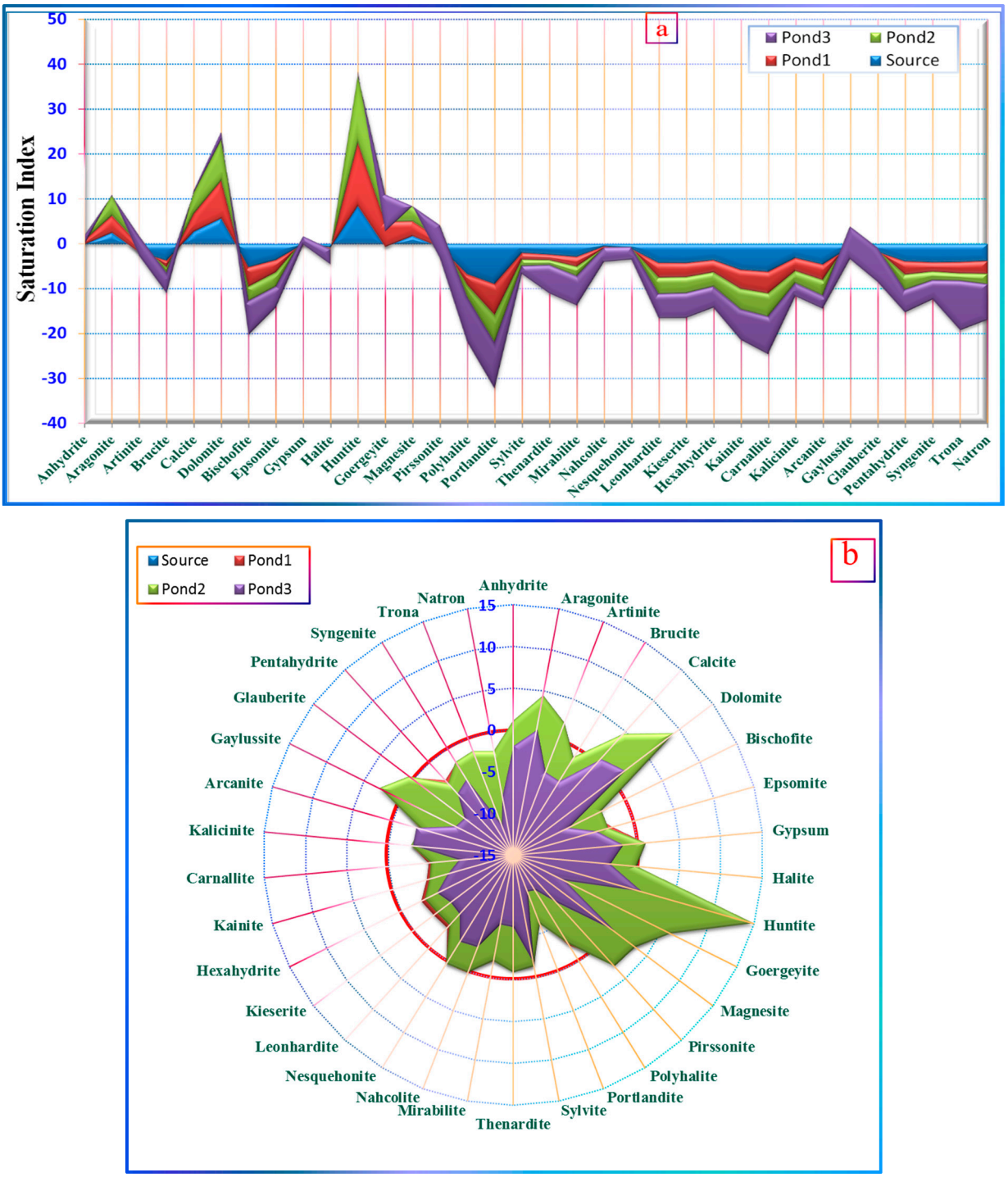

Figure 14. Area plot (**a**) and radar plot (**b**) of the SIs of mineral assemblages.

Despite the purity of the harvested halite, such a theme may guide improving the current folkloric harvesting process to provide halite of superior purity without the need for further purification and qualify the system to provide a readily available feed intake to the electrolysis chlor-alkali process without or with minimal pretreatment when used to produce higher value chemicals, NaOH, HCl, NaOCl, Cl_2, and H_2. The detailed description and feasibility of such chlor-alkali processes are beyond the scope of the current work. The conceptually proposed system (Figure 16) is based on giving enough time and an appropriate flow regime to allow precipitation of the minerals with the highest SIs in pond 1 and pond 2, and pond 2 should have a higher shape factor (length-to-width ratio) that

might result in a semi-plug-flow regime with lower chances of eddy formation, allowing the settlement of the crystallized phases. Moreover, this pond 2 design is claimed to result in no halite saturation and could result in faster transfer to the subsequent pond thanks to its higher mobility. As such, pond 3 is claimed to have quasi-saturated brine with halite and without the other scale-forming minerals. With the progression of evaporation, the brine becomes saturated, halite is crystallized, and the supernatant passes to pond 4. In turn, with evaporation, pond 4 becomes saturated, and halite is separated again. The remaining brine going to pond 5 is now concentrated with mirabilite and sylvite. Cooling could crystallize mirabilite ($Na_2SO_4 \cdot 10H_2O$), and the final solution could evaporate until another portion of halite is separated. The sylvite experiences higher repeated concentration factors through this brine-sequestration process that might be feasible enough to promote its separation.

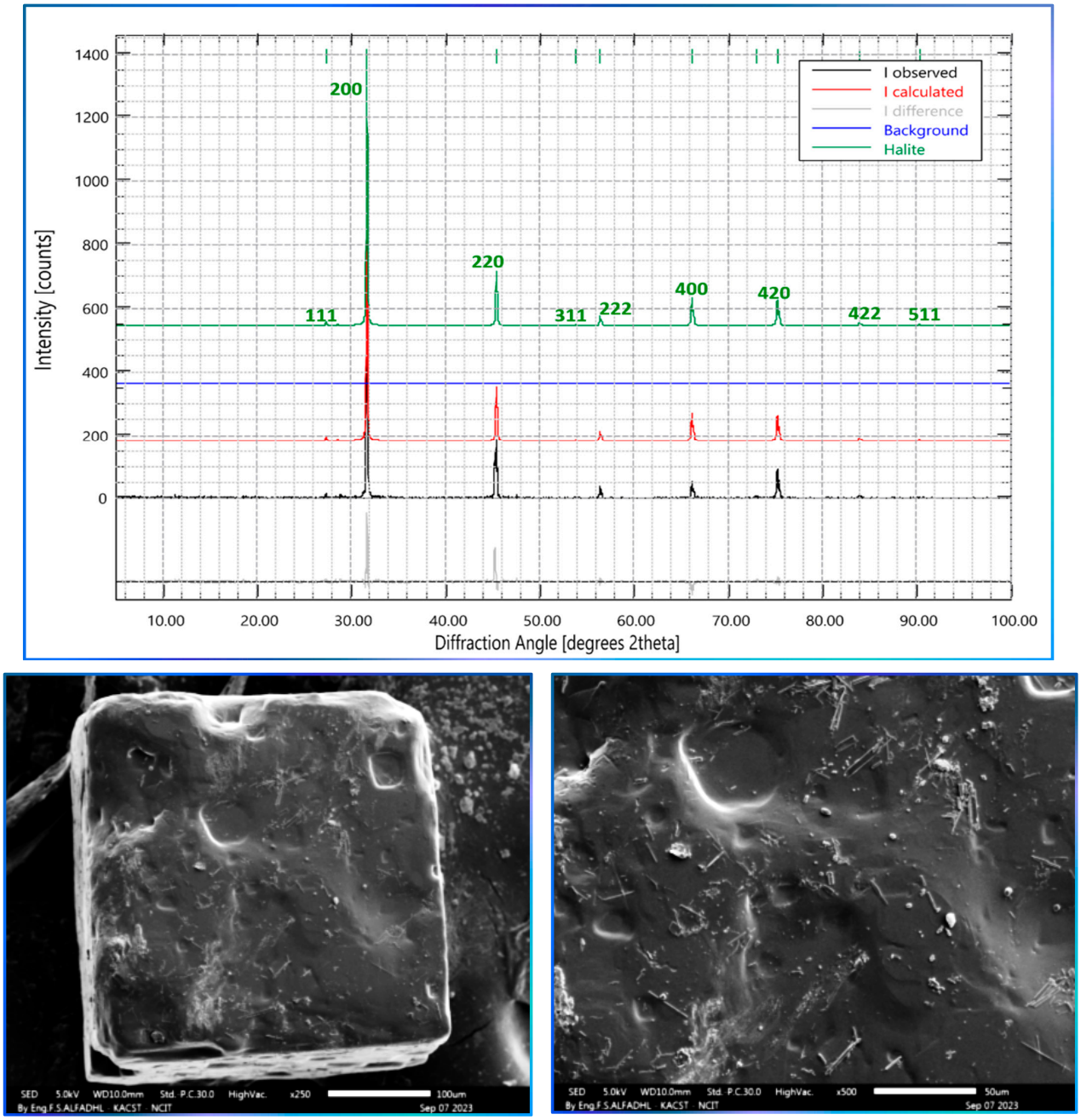

Figure 15. X-ray diffraction spectra and SEM of the halite harvested from pond 3.

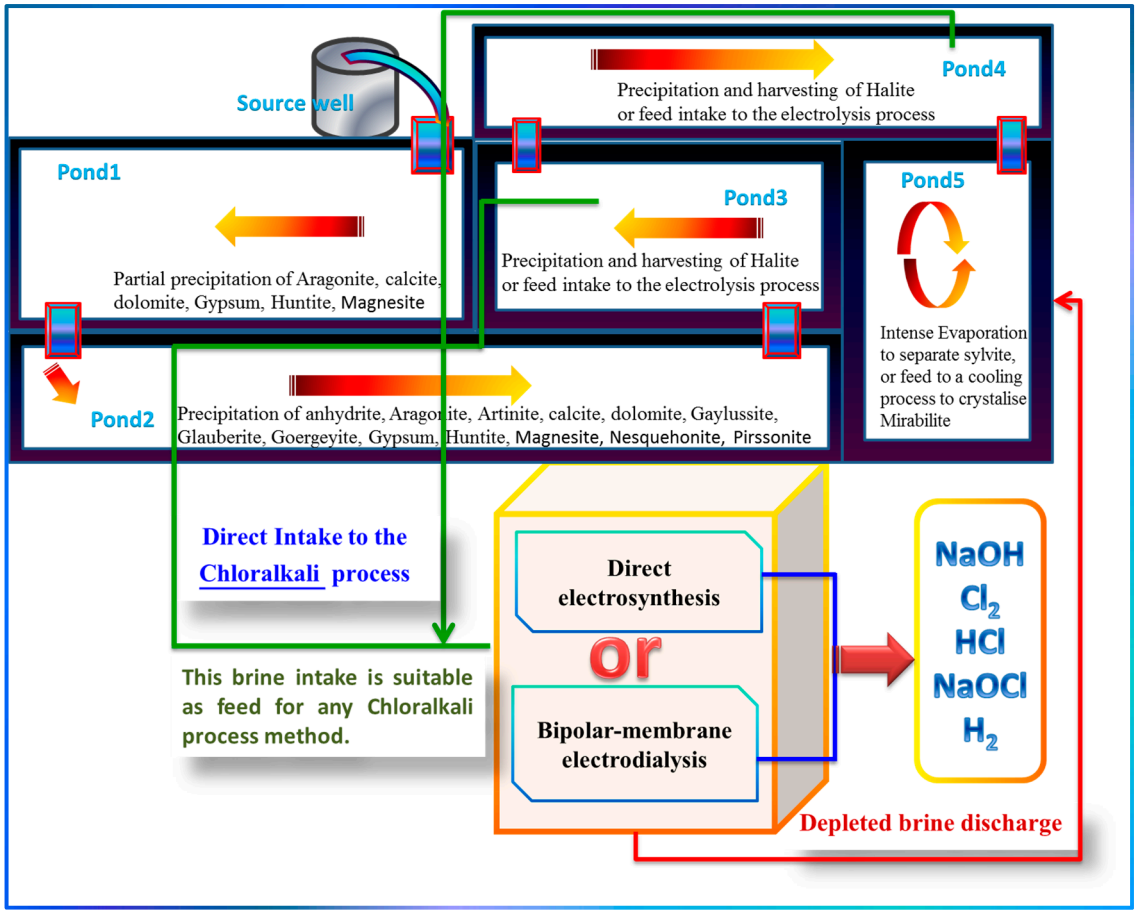

Figure 16. A conceptually improved design of the solar evaporation ponds to provide a readily available feed intake for the chlor-alkali process.

3.6. Climatic Conditions

The region's climatic conditions are hyperarid and very hot in summer, which are considered favorable for a rapid solar evaporative concentration process. The maximum yearly average precipitation during the period from 1985 to 2015 is 5 mm, with a wind speed of 11.15 Km/h; mean high and low temperatures of 34 °C and 19 °C, respectively; a maximum high temperature of 44 °C; and a mean humidity of 25%. The climatic conditions in the region are summarized in Figure 17. Overall, the climatic conditions are best from the evaporative concentration point of view.

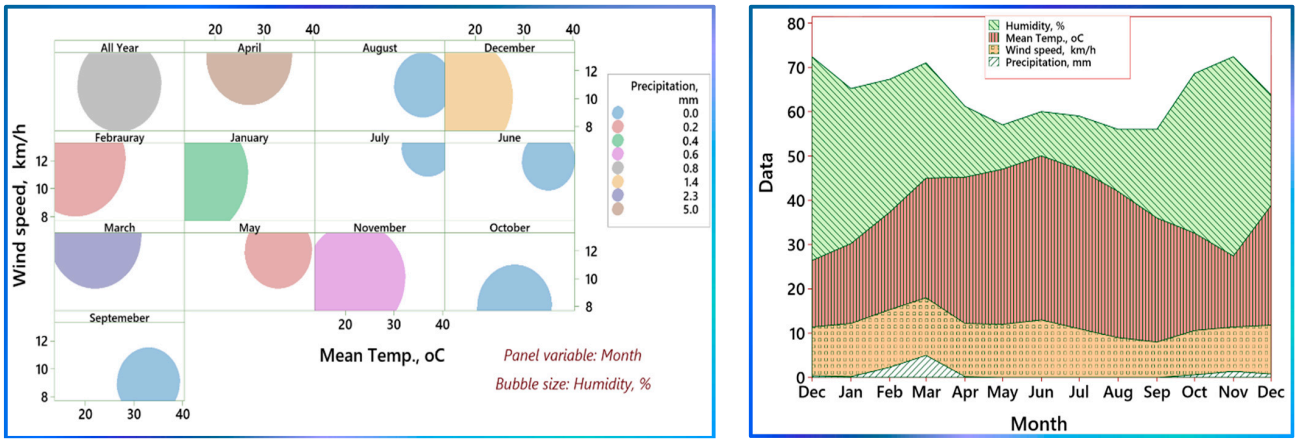

Figure 17. Summary of the climatic conditions in the region during the period from 1985 to 2015 [43].

4. Conclusions

In this study, a diverse set of approaches, including ArcGIS-processed SRTM-DEM data, hydrogeochemical, thermodynamic-based Geochemical Modeling, and graphical approaches, have been integrated conceptually and quantitively when possible to evaluate the sustainability of the halite harvesting process from Al-Qassab Playa, Shaqra, Central Saudi. The study integrated, complemented, declined and/or corroborated the conclusions of each approach to identify the controls and sources of the bring geochemical evolution. The main conclusions could be summarized as follows:

a. The SRTM-DEM information indicates that the Al-Qasab watershed is a nonmarine closed basin with a drainage watershed area of 1290 km^2, which is considerably large enough to secure a long-term supply of salts, as confirmed through its continuous operation from the Chrestician seventh century until now. The slope and relative elevation parameters control recharge to the Playa watershed with the harvesting solar evaporation ponds being ≈30 km^2 in area.
b. The linear regression coefficients for EC or TDS for the pond with the source well water (considered pond 1) was 0.696. The concentration changes at ponds 2 and 3 were mild, which may be ascribed to the precipitation of some constituents reaching their solubility limits and the negative effect of concentration on the vaporization tendency according to Raoult's law.
c. The relationship of EC and TDS with the pond number followed a polynomial regression (i.e., the extent of evaporation) with R^2 values of 0.9491 and 0.946, respectively, indicating the significant impact of evaporation on the source well water.
d. The Chadha plot reveals a perfect fit of the linear regression, with an R^2 value of 0.9947 including the rainwater, source well water, and pond 1 and pond 2 samples, confirming the rainwater origin of the source water as they fit with pond 1 and pond 2, which were exposed to vigorous solar evaporation.
e. The hardness-forming ions are primarily removed in pond 3, eliminating the need for costly and power-consuming steps of softening using ion exchange resins or nanofiltration as it can be used directly as a readily available feed for the chlor-alkali process for producing NaOH, Cl_2, and H_2 gases through electrolysis.
f. The climatic conditions in the region are best from the evaporative concentration point of view, allowing the establishment of feasible evaporation rates in due time courses to plan an industrial process.
g. The XRD spectra and the SEM-EDS of the harvested halite confirmed its purity with only one cubic phase of cubic halite with a unit cell of Cl4Na4 and a cell parameter (a) of 0.56423, providing pure salt.
h. Pond 2 in the current operating folkloric pond design demonstrated the highest SIs, even for halite.
i. An improved design of the current folkloric methodology has been proposed conceptually based on the SI calculated thermodynamically to provide a readily available feed intake for the chlor-alkali electrolysis process with or without minimal pretreatment.

The methodological aspects presented here are deemed robust and valid for application to other study areas, including the assessment of the exploitation of the rejected brine from the desalination plants to achieve the zero liquid discharge goal and for the other types of sabkhas, regardless of their geographical locations.

Supplementary Materials: The following supporting information can be downloaded at: https://www.mdpi.com/article/10.3390/su16052118/s1, Figure S1: Areal view of the study area and the solar evaporation ponds; Figure S2: Relationship between Na^+/Cl^- ratio and EC (a) and that of the total cations versus Na + K in mEq/L.

Author Contributions: H.E.G.: Conceptualization, Methodology, Software, Validation, Formal Analysis Investigation, Resources, Data Curation, Writing-Original Draft Preparation, Supervision, Project Administration, Funding Acquisition. F.A.G.: Conceptualization, Methodology, Software, Investi-

gation, Data Curation, Writing-Original Draft Preparation, Writing-Review, and Editing. S.M.A.A.: Methodology, Validation, Formal Analysis, Writing-Review, and Editing. A.A.A.: Methodology, Validation, Resources, Data Curation, Writing-Review, and Editing. All authors have read and agreed to the published version of the manuscript.

Funding: The authors extend their appreciation to Shaqra University for funding this research work.

Institutional Review Board Statement: Not applicable.

Informed Consent Statement: Not applicable.

Data Availability Statement: Data is contained within the article and Supplementary Materials.

Conflicts of Interest: The authors declare no conflicts of interest. The funders had no role in the design of the study; in the collection, analyses, or interpretation of data; in the writing of the manuscript; or in the decision to publish the results.

References

1. Al-Harbi, O.; Hussain, G.; Khan, M. Sedimentology, Mineralogy and Geochemistry of Al-Awshaziyah Inland Sabkha, Central Saudi Arabia. *Arid Land Res. Manag.* **2006**, *20*, 117–132. [CrossRef]
2. Al-Saafin, A.K. The Characterization of Sabkhas in the Eastern Parts of Saudi Arabia and Its Implications for Engineering. Ph.D. Thesis, Queen Mary University of London, London, UK, 1996; p. 316.
3. Kolodny, Y. *Hypersaline Ecosystems, The Gavish Sabkha*; Springer: Berlin/Heidelberg, Germany, 1986; Volume 50, ISBN 9783642702921.
4. AL-Amoudi, O.S.B.; Aiban, S.A.; Al-Abdul Wahhab, H.I. Variability and Characteristics of Eastern Saudi Sabkha Soils. In Proceedings of the International Conference on Soil Mechanics and Foundation Engineering, Hamburg, Germany, 6–12 September 1997; pp. 17–20. Available online: https://www.issmge.org/publications/publication/variability-and-characteristics-of-eastern-saudi-sabkha-soils (accessed on 7 February 2024).
5. Chatterjee, B.C.; Sarma, N.; Sahu, P.P.; Oki, E. Literature Survey. *Lect. Notes Electr. Eng.* **2017**, *410*, 17–34. [CrossRef]
6. Sabtan, A.A.; Shehata, W.M. Problematic Sabkha—A Potential Source of Fresh Water. *Bull. Eng. Geol. Environ.* **2002**, *61*, 153–159. [CrossRef]
7. All, K.; Hossain, D. Geotechnical and Geochemical Characteristics of Obhor Sub-Soil. *J. King Abdulaziz Univ. Sci.* **1988**, *1*, 205–225. [CrossRef]
8. Sabtan, A.A.; Shehata, W.M. Hydrogeology of Al-Lith Sabkha, Saudi Arabia. *J. Asian Earth Sci.* **2003**, *21*, 423–429. [CrossRef]
9. Ye, C.; Mao, J.; Ren, Y.; Li, Y.; Lin, Y.; Power, I.M.; Luo, Y. Salt Crystallization Sequences of Nonmarine Brine and Their Application for the Formation of Potassium Deposits. *Aquat. Geochem.* **2018**, *24*, 209–229. [CrossRef]
10. Taj, R.J.; Aref, M.A. Structural and Textural Characteristics of Surface Halite Crusts of a Supratidal, Ephemeral Halite Pan, South Jeddah, Red Sea Coast, Saudi Arabia. *Facies* **2015**, *61*, 2. [CrossRef]
11. Attia, O.E.A. Sedimentological Characteristics and Geochemical Evolution of Nabq Sabkha, Gulf of Aqaba, Sinai, Egypt. *Arab. J. Geosci.* **2013**, *6*, 2045–2059. [CrossRef]
12. Manning, C.E.; Aranovich, L.Y. Brines at High Pressure and Temperature: Thermodynamic, Petrologic and Geochemical Effects. *Precambrian Res.* **2014**, *253*, 6–16. [CrossRef]
13. Akili, W. *Scholars' Mine Foundations over Salt-Encrusted Flats (Sabkha): Profiles, Properties, and Design Guidelines*; IFCEE: Dallas, TX, USA, 2004; pp. 1–9.
14. Hussain, M.; Al-Shaibani, A.; Al-Ramadan, K.; Wood, W.W. Geochemistry and Isotopic Analysis of Brines in the Coastal Sabkhas, Eastern Region, Kingdom of Saudi Arabia. *J. Arid Environ.* **2020**, *178*, 104142. [CrossRef]
15. Saeed, W.; Shouakar-Stash, O.; Unger, A.; Wood, W.W.; Parker, B. Chemical Evolution of an Inland Sabkha: A Case Study from Sabkha Matti, Saudi Arabia. *Hydrogeol. J.* **2021**, *29*, 1939–1951. [CrossRef]
16. Hidayatulloh, A.; Chaabani, A.; Zhang, L.; Elhag, M. DEM Study on Hydrological Response in Makkah City, Saudi Arabia. *Sustainability* **2022**, *14*, 13369. [CrossRef]
17. Rahman, M.M.; Arya, D.S.; Goel, N.K. Limitation of 90 m SRTM DEM in Drainage Network Delineation Using D8 Method-a Case Study in Flat Terrain of Bangladesh. *Appl. Geomat.* **2010**, *2*, 49–58. [CrossRef]
18. Available online: https://Earthexplorer.Usgs.Gov (accessed on 7 February 2024).
19. Quevauviller, P.; Thompson, K.C. *Analytical Methods for Drinking Water*; John Wiley & Sons: Hoboken, NJ, USA, 2005; ISBN 9780470094938.
20. DPIR Methodology for the Sampling of Surface Water. *North. Territ. Gov.* **1998**, *11*, 1–11.
21. UGSS. *National Field Manual for the Collection of Water-Quality Data. U.S. Geological Survey Techniques of Water-Resources Investigations, Book 9*; UGSS: Reston, VA, USA, 2015.
22. APHA. *Standard Methods: For the Examination of Water and Waste Water*, 23rd ed.; Rodger, B., Andrew, E., Rice, E., Eds.; American Public Health Association: Washington, DC, USA, 2017.
23. Middleton, K.R. A New Procedure for Rapid Determination of Nitrate and a Study of the Preparation of the Phenol-Sulphonic Acid Reagent. *J. Appl. Chem.* **1958**, *8*, 505–509. [CrossRef]

24. Gomaa, H.E.; Alotibi, A.A.; Charni, M.; Gomaa, F.A. Integrating GIS, Statistical, Hydrogeochemical Modeling and Graphical Approaches for Hydrogeochemical Evaluation of Ad-Dawadmi Ground Water, Saudi Arabia: Status and Implications of Evaporation and Rock–Water Interactions. *Sustainability* **2023**, *15*, 4863. [CrossRef]
25. Abdelkader, M.M.; Al-amoud, A.I.; El, M.; El-feky, A. Remote Sensing Applications: Society and Environment Assessment of Flash Flood Hazard Based on Morphometric Aspects and Rainfall-Runoff Modeling in Wadi Nisah, Central Saudi Arabia. *Remote Sens. Appl. Soc. Environ.* **2021**, *23*, 100562.
26. Raja Shekar, P.; Mathew, A. Morphometric Analysis of Watersheds: A Comprehensive Review of Data Sources, Quality, and Geospatial Techniques. *Watershed Ecol. Environ.* **2024**, *6*, 13–25. [CrossRef]
27. Bogale, A. Morphometric Analysis of a Drainage Basin Using Geographical Information System in Gilgel Abay Watershed, Lake Tana Basin, Upper Blue Nile Basin, Ethiopia. *Appl. Water Sci.* **2021**, *11*, 122. [CrossRef]
28. Sukristiyanti, S.; Maria, R.; Lestiana, H. Watershed-Based Morphometric Analysis: A Review. *IOP Conf. Ser. Earth Environ. Sci.* **2018**, *118*, 012028. [CrossRef]
29. Chadha, D.K. A Proposed New Diagram for Geochemical Classification of Natural Waters and Interpretation of Chemical Data. *Hydrogeol. J.* **1999**, *7*, 431–439. [CrossRef]
30. Piper, A.M. A Graphic Procedure in the Geochemical Interpretation of Water-Analyses. *Transcation, Am. Geophys. Union* **1944**, *25*, 914–928.
31. Alabdula'aly, A.I.; Khan, M.A. Chemistry of Rain Water in Riyadh, Saudi Arabia. *Arch. Environ. Contam. Toxicol.* **2000**, *39*, 66–73. [CrossRef] [PubMed]
32. Lorenz, D. Piper Plot and Stiff Diagram Examples. 2016; pp. 1–9. Available online: https://pubs.usgs.gov/of/2016/1188/downloads/ofr20161188_appendix8.pdf (accessed on 15 January 2024).
33. Güler, C.; Thyne, G.D.; Mccray, J.E.; Turner, A.K. Evaluation of Graphical and Multivariate Statistical Methods for Classification of Water Chemistry Data. *Hydrogeol. J.* **2002**, *10*, 455–474. [CrossRef]
34. Adimalla, N.; Kumar, S.; Peiyue, V. Evaluation of Groundwater Quality, Peddavagu in Central Telangana (PCT), South India: An Insight of Controlling Factors of Fluoride Enrichment. *Model. Earth Syst. Environ.* **2018**, *4*, 841–852. [CrossRef]
35. AlSuhaimi, A.O.; AlMohaimidi, K.M.; Momani, K.A. Preliminary Assessment for Physicochemical Quality Parameters of Groundwater in Oqdus Area, Saudi Arabia. *J. Saudi Soc. Agric. Sci.* **2019**, *18*, 22–31. [CrossRef]
36. Chidambaram, S.; Anandhan, P.; Prasanna, M. V Major Ion Chemistry and Identification of Hydrogeochemical Processes Controlling Groundwater in and around Neyveli Lignite Mines, Tamil Nadu, South India. *Arab. J. Geosci.* **2012**, *6*, 3451–3467. [CrossRef]
37. Feth, J.H.; Gibbs, R.J. Mechanisms Controlling World Water Chemistry: Evaporation-Crystallization Process. *Am. Assoc. Adv. Sci. Stable* **1971**, *172*, 870–872. [CrossRef]
38. Bouwer, H. Irrigation and Global Water Outlook. *Natl. Conf. Publ. Inst. Eng. Aust.* **1994**, *2*, 221–231. [CrossRef]
39. Thiel, G.P.; Kumar, A.; Gómez-González, A.; Lienhard, J.H. Utilization of Desalination Brine for Sodium Hydroxide Production: Technologies, Engineering Principles, Recovery Limits, and Future Directions. *ACS Sustain. Chem. Eng.* **2017**, *5*, 11147–11162. [CrossRef]
40. Kumar, A.; Phillips, K.R.; Thiel, G.P.; Schröder, U.; Lienhard, J.H. Direct Electrosynthesis of Sodium Hydroxide and Hydrochloric Acid from Brine Streams. *Nat. Catal.* **2019**, *2*, 106–113. [CrossRef]
41. Hine, F.; O'Brien, T.F.; Bommaraju, T.V. *Handbook of Chlor-Alkali Technology, Volume I: Fundamentals*; Springer: Berlin/Heidelberg, Germany, 2005; ISBN 2381970770.
42. USGS PhreeqC. Available online: https://www.usgs.gov/software/phreeqc-version-3 (accessed on 22 February 2024).
43. Climate & Weather Averages in Riyadh, Saudi Arabia. Available online: https://www.timeanddate.com/weather/saudi-arabia/riyadh/climate (accessed on 15 January 2024).